Neutral Atom Lithography Using the 389 nm Transition in Metastable Helium

A Dissertation Presented

by

Jason Reeves

to

The Graduate School

in Partial Fulfillment of the Requirements

for the Degree of

Doctor of Philosophy

in

Physics

Stony Brook University

August 2010

Neutral Atom Lithography Using the 389 nm Transition in Metastable Helium

A Dissertation Presented

by

Jason Reeves

to

The Graduate School

in Partial Fulfillment of the Requirements

for the Degree of

Doctor of Philosophy

in

Physics

Stony Brook University

August 2010

Stony Brook University

The Graduate School

Jason Reeves

We, the dissertation committee for the above candidate for the Doctor of Philosophy degree, hereby recommend acceptance of this dissertation.

Harold Metcalf – Dissertation Advisor
Distinguished Teaching Professor, Department of Physics and Astronomy

Dominik Schneble – Chairperson of Defense
Assistant Professor, Department of Physics and Astronomy

Derek Teaney
Assistant Professor, Department of Physics and Astronomy

Jon Longtin
Associate Professor, Department of Mechanical Engineering
SUNY Stony Brook

This dissertation is accepted by the Graduate School.

Lawrence Martin
Dean of the Graduate School

Abstract of the Dissertation

Neutral Atom Lithography Using the 389 nm Transition in Metastable Helium

by

Jason Reeves

Doctor of Philosophy

in

Physics

Stony Brook University

2010

Resist based neutral atom lithography with metastable 2^3S_1 Helium (He*) has been used to produce small structures in both gold and palladium. A beam of He* from a reverse flow, DC discharge source is collimated by the bichromatic optical force followed by three optical molasses velocity compression stages. The He* beam then crosses a region where a mechanical or optical mask creates the desired pattern.

In the first experiments, a self assembled monolayer (SAM) of nonanethiol is grown on a gold coated silicon wafer and then exposed to the bright, collimated beam of He* after a nickel micro

mesh mask. The mesh protects parts of the SAM from the 20 eV of internal energy deposited by the impact of a He* atom onto the sample surface. The pattern of the mesh is transferred into the ∼200 Å gold layer with a standard selective etch that removes the gold from under the damaged SAM molecules. The samples were analyzed with an Atomic Force Microscope and Scanning Electron Microscope.

The second set of experiments were performed using an optical mask to pattern a gold coated silicon wafer. In the optical mask, the He* atoms experience the dipole force while traversing a standing light wave of $\lambda_1 = 1083$ nm light tuned 490 MHz above the $2^3S_1 \rightarrow 2^3P_2$ transition or, in separate experiments, $\lambda_2 = 389$ nm light tuned 80 MHz below the $2^3S_1 \rightarrow 3^3P_2$ transition. Using the optical masks, He* can be focused or channeled into parallel lines separated by $\lambda/2$ by varying the intensity of the standing light wave.

The small structures created by the 389 nm optical mask began approaching the gold surface granularity. A ∼ 200Å layer of palladium on silicon was chosen as the palladium granularity is much smaller and the SAM of nonanethiol will still form on the surface. Experiments using a nickel micro mesh as a mechanical mask have demonstrated similar features to those in gold.

For my family and friends

Contents

List of Figures

List of Tables

Acknowledgements

After six full years of graduate school, my time at Stony Brook is quickly coming to a close. Graduating is an interesting time to reminisce about all the adventures that occurred in graduate school. I want to say thank you to everyone who has helped me in my journey and, although by no means will it be a complete list, thank a few people by name.

The first person that I would like to thank is my advisor, Hal Metcalf. I joined his group five years ago and, looking back, I still consider myself lucky. Hal has a love for physics that is contagious to all of the people around him. He sees the potential in people and is a truly amazing teacher. He somehow manages to allow his students to make their own mistakes while always being there to provide guidance and new ideas to keep the research going. Although pages could be written to describe how great it has been to work for Hal, I will just say that I am very thankful that I was able to spend the last five years in his lab.

Over the last five years, the people that I saw most were my colleagues. When I started, Claire Allred took me under her wing and taught me the basics about the lab. We got to experience the emotional lows of many failures and the excitement of first results together. Claire taught me many things and I am very grateful that I was able to work with such an incredibly interesting person. I am indebted to her for laying the groundwork for my thesis. Near the end of my career, I have had the privilege of working with Chris Corder. Chris has a keen sense of what questions to ask to get to the heart of the problem and is a great physicist. I leave the lab knowing he will do great things and am thankful for all of the hours he spent helping me finish my graduate career.

The other people in lab have also been a huge part of my life over the last several years. Xiaoxu Lu joined the group a year after I did and has built an experiment from scratch. Her hard work and perseverance will serve her well in whatever she does in the future. John Elgin has been a great lab mate and has provided plenty of exercise on our long bike rides. Dan Stack and Yuan Sun have been a lot of fun to work with and I wish them well also.

I also want to take a moment to mention all those physicists that I had the privilege of working with throughout the rest of my graduate career. A special thank you is extended to all the Germans who were a part of the exchange program. I would also like to thank Marty Cohen who provided many great ideas and a lot of advice on many of the problems that would arise in lab.

As a graduate student, I was lucky to be able to concentrate on just doing physics. This was in large part thanks to Hal and Linda Dixon who took care of all the administrative work for the group. When it was out of their hands, we have a very capable office staff who worked hard to keep everything running smoothly. I would like to thank the entire office staff including Sara Lutterbie, Diane Diaferia, Pam Burris and Elaine Larsen. A special thanks goes to Pat Peiliker for the many years that she put in to helping graduate students like me survive.

I also want to thank all the people that keep things in lab working. Bob Segnini and Richard Berscak did wonders to keep the building maintained. The electronics shop is staffed by two very talented people, Chuck Pancake and Gene Shafto. The many talks with Gene were both enlightening and fun. Paul, Mark, Walter, Jeff and J.T. worked in the machine shop and did some incredible machining for us and I thank them. A big thanks goes to Pete Davis who could fix almost anything we broke.

I would also like to thank the people that made my time outside of school enjoyable. I cannot imagine the past few years without the support and friendship of the Dusling family, the Lapidus family, Clint Young and Julie Elder. I had the chance to swim with the Seawolves Masters team and I thank them for the many early mornings with a special thanks to Jim and Maria Anderson. I also thank my church in Coram for six wonderful years.

I want to thank my parents for their unconditional support and love throughout my adventures in graduate school. I also want to thank my wife for her love and patience as I finished writing this document in the weeks before our wedding.

Thank you all!

Chapter 1

Introduction

Since the invention of the laser 50 years ago, atomic physicists have made large advances in the understanding and control of atoms. The laser enabled people to study atomic spectroscopy and learn about the electronic structure of the atom. With more knowledge of atom-light interactions, the atomic physics field grew rapidly.

Laser cooling is one major part of atom-light interactions. A laser can be used to apply forces to atoms, and by exploiting the Doppler shift, can even be used to slow an atoms velocity. Experiments with standing light waves in three dimensions were done which slowed atomic velocities to a few cm/s. By using magnetic fields along with light fields, physicists were able to not only slow the atoms but trap them as well. These experiments would lead to the first Bose-Einstien condensate.

In 1992, a standing light wave traversed an atomic beam of sodium and affected the atomic trajectories [1]. The atoms landed in parallel lines separated by half the wavelength of the standing wave. This was the first neutral atom lithography experiment.

Neutral atom lithography (NAL) has some advantages over other common lithographic techniques. NAL does not suffer from the charge/space issue that limit the feature size of both electron beam and ion lithography. NAL also has the ability to produce areas of highly periodic structures, based on the properties of the light. Electron beam lithography requires great care to raster the beam properly to limit errors in spacing. In contrast to photolithography, NAL is limited not by the wavelength of the light but by the properties of the atom.

The first experiment in 1992 served as a proof of principle and in 1993 was done using chromium instead of sodium [2]. The advantage is that chromium could be taken out of the vacuum system, as it is not nearly as reactive to air as sodium. Both of these experiments required the atom to interact with the light field and then be directly deposited onto a substrate. The resulting direct deposit could be measured by diffraction, atomic force microscopes or scanning electron microscopes depending on the set up.

In 1995, a technical advance came when it was realized that neutral atom lithography could be accomplished by using the internal energy of the atoms to damage a sample coated with a resist [3]. The major advance is that once the control of an atomic beam is obtained, the final features can be etched into any material that has a suitable resist/etch.

The purpose of this work is to perform resist assisted NAL with metastable Helium atoms. The metastable state in Helium has the greatest amount of energy of any atom and will help in short etching times. However, creating metastable Helium is not trivial and we will use standard laser cooling techniques to capture and slow as many atoms as possible.

The thesis will be broken down into four basic sections: 1)A short review of the quantum mechanics of an atom in a light field 2)A review of the laser cooling techniques used to collimate the atomic beam 3) An experimental section which explains how the light and atoms are produced and gives the details about the lithographic exposures and 4)the results that were achieved in the laboratory.

In 15 years of resist based NAL, metastable Helium has been used to make shadows of mechanical masks and features created by high powered 1083 nm optical masks in gold. In continuation of work done with a previous thesis, this work has demonstrated features in the low power regime of the 1083 nm optical mask [4]. New results include steering atoms with a 389 nm optical mask which gives the smallest resist-assisted parallel lines to date. This work also includes the first time palladium has been patterned by metastable Helium atoms using resist-assisted NAL.

1.1 Schrödinger Equation

The Schrödinger equation for a bound electron is

$$\mathcal{H}\Psi = -\left(\frac{\hbar^2}{2m}\nabla^2 - V\right)\Psi = i\hbar\frac{\partial\Psi}{\partial t} \tag{1.1}$$

where Ψ is the atomic wave function, $\mathcal{H}$ is the Hamiltonian, m is the electron mass and V is the potential. Solutions to this equation where $V = -\frac{e^2}{r}$ have been given in several places [5, 6].

The solution that concerns the current work of this thesis is one for the Helium atom. Hans Bethe and Edwin Salpeter, described this problem in 1957 [7] and the following is a brief review of their work. By using $\Psi(r_1, r_2, t) = \psi(r_1, r_2)e^{-iEt/\hbar}$ to include the time dependence of the wave function explicitly, the time independent Schrödinger equation for a two proton nucleus and two electrons becomes

$$\left[\frac{\hbar^2}{2m_e}\left(\nabla_1^2 + \nabla_2^2\right) + \frac{Ze^2}{r_1} + \frac{Ze^2}{r_2} - \frac{e^2}{r_{1,2}} + E\right]\psi(r_1, r_2) = 0 \tag{1.2}$$

where the nuclear charge Z=2, r_1 and r_2 refer to the distance between the respective electrons and the nucleus and $r_{1,2}$ is the separation between the two electrons. ∇_1 refers to the x_1, y_1, z_1 coordinate system of the first electron and ∇_2 refers to x_2, y_2, z_2 coordinate system of the second electron. In Eq. (1.2), ψ is a function of all six spatial coordinates but is independent of time.

The Helium atom has symmetries that will be reflected in the properties of the solution. If the two electrons are exchanged, the solution must satisfy the same differential equation, since they are identical particles. If the electrons are interchanged again, the wave function must return to the original solution. These two properties require

$$\psi(r_2, r_1) = \pm\psi(r_1, r_2) \tag{1.3}$$

The preceding equation gives rise to what are referred to as *para* (symmetric eigenfunctions) and *ortho* (antisymmetric eigenfunctions) helium.

The spin of the electrons must also be considered since each electron can have spin of $S_z = \pm\frac{1}{2}$ with respect to a fixed z-direction. The spin wave function must also be either symmetric or antisymmetric, and combined with the Pauli exclusion principle requires the following four spin wave functions:

$$\left.\begin{aligned} S_+ &= \alpha(1)\alpha(2), \qquad S_- = \beta(1)\beta(2), \\ S_0 &= \tfrac{1}{\sqrt{2}}\Big[\alpha(1)\beta(2) + \beta(1)\alpha(2)\Big] \end{aligned}\right\} \tag{1.4}$$

$$S_P = \frac{1}{\sqrt{2}}\Big[\alpha(1)\beta(2) - \beta(1)\alpha(2)\Big] \tag{1.5}$$

where α refers to the $+\frac{1}{2}$ spin state, β refers to the $-\frac{1}{2}$ spin state and the number in the parenthesis refers to the electron. The first three spin wave functions, Eq. (1.4), are all symmetric with respect to exchanging the electron labels. To keep the overall wave function antisymmetric, these three symmetric spin wave functions must be multiplied by an antisymmetric spatial wave function. The resulting complete wave functions are referred to as triplet states or *ortho*helium. The last spin state, Eq.(1.5), must be multiplied by a symmetric spatial wave function. In mathematical terms, these amount to $\Phi(r_1, r_2, s_1, s_2) = \psi(r_1, r_2)\chi(s_1, s_2) = -\Phi(r_2, r_1, s_2, s_1)$ where ψ is the spatial part of the wave function and χ is the spin component of the wave function.

The analysis presented above all comes from the analysis of a two-electron system and has not solved Schrödinger's equation for the Helium wave functions. Bethe and Salpeter provide an excellent discussion of different approximations and numerical methods that allow the wave functions and excited states of Helium to be estimated. For brevity, three approaches will be described as in Metcalf's class notes on atomic physics.

The first approach is to ignore the inter-electron repulsion $\frac{e^2}{r_{1,2}}$ term. This makes the differential equation analytically solvable, but the approximation is not entirely physically justified. The spatial wave functions can be separated by the substitution $\psi(r_1, r_2) = u(r_1)v(r_2)$ into Eq. (1.2). Written in spherical coordinates, $u(r_1)$ and $v(r_2)$ are each products of a radial $R_{n,\ell}(r)$ and an angular $Y_{\ell,m}(\theta,\phi)$ wave function with different subscripts. The substitution leads to two separate equations, one for each $u(r_1)$ and $v(r_2)$. Each wave function is just the solution to the Hydrogen atom with Z=2, so that the energy of the ground state of Helium should be eight times the Hydrogen atom's ground state energy

$$E_{gs} = \left(-\frac{m_e c^2}{2}\frac{4\alpha^2}{n^2}\right) \times 2 = -108.8 \ \ eV. \tag{1.6}$$

with the fine structure constant $\alpha \equiv \frac{e^2}{4\pi\epsilon_0\hbar c} \sim \frac{1}{137}$.

The second approach is to treat the $\frac{e^2}{r_{1,2}}$ term as a perturbation to the system. The energy shift of the ground state given by first order perturbation theory, with the trial wave function $R_1(r_1)Y_{0,0}(\theta_1,\phi_1)R_1(r_2)Y_{0,0}(\theta_2,\phi_2)$, is

$$\Delta E^{(1)}_{g,s} = \int \left|\Psi_{gs}\right|^2 \frac{e^2}{r_{1,2}} d^3r_1 d^3r_2 = \frac{Z^6 e^2}{\pi^2 a_0^6} \int \frac{e^{-2Z(r_1+r_2)/a_0}}{\left|\vec{r_1} - \vec{r_2}\right|} d^3r_1 d^3r_2 \tag{1.7}$$

where $a_0 = \frac{\hbar}{m_e c\alpha}$. Although the integral is not trivial, it can be solved by expanding the $\frac{e^2}{r_{1,2}}$ term in Legendre polynomials. Using the properties of the Legendre polynomials, the integral results in

$$\Delta E^{(1)}_{g,s} = \frac{Z^6 e^2}{\pi^2 a_0^6}\frac{5\pi^2 a_0^5}{8Z^5} = \frac{5}{4}Z\big(\frac{m_e c^2\alpha^2}{2}\big) = +34.0eV. \tag{1.8}$$

The first order perturbation is a significant fraction of the ground state energy found in Eq. (1.6), but the combined value of $-74.8\ eV$ is much closer to the experimentally measured value of $-78.97\ eV$.

The third approach is to consider Coulombic screening of the nucleus from the two electrons by modifying the spatial wave function. The hydrogen atom only has one electron and screening cannot occur, but for other atoms it is an important effect that should be considered. Since an inner electron will screen the nucleus of the atom from an outer electron, it is useful to change $\psi(r_1, r_2) \sim e^{-Z(r_1+r_2)/a_0}$ to $\psi(r_1, r_2) \sim e^{-\beta(r_1+r_2)}$. The energy can now be recalculated while allowing the effective nuclear charge, β, to vary. Rewriting Eq. (1.2) in the form $\mathcal{H}\psi = E\psi$ and calculating the expectation value of H yields

$$< \mathcal{H} >= e^2(\beta^2 a_0 - 2\beta Z + \frac{5}{8}\beta). \tag{1.9}$$

Minimizing this with respect to β yields

$$\beta = \frac{27Z}{32a_0}. \tag{1.10}$$

Substituting the minimum value of β into Eq.(1.9), gives the very close result of -77.41 eV. The calculated value from this approach is only $1.56\ eV$ from the measured value.

The energies and the wave functions of the excited states of *ortho*Helium can be calculated and closely resemble the energy level diagram that can be seen in Figure (1.1). Finding the excited states of Helium is a worthwhile task but will not be pursued here since approximating the $2^3S_1 - 2^3P_2$ and the $2^3S_1 - 3^3P_2$ states each as two level systems describes the current experiments well. The details of this approximation are discussed in the next section.

In this experiment, the ground state of the two level atom will be the metastable 2^3S_1 state because it has an extremely long lifetime of $\tau = 7900$ s [8], where the lifetime is only limited by relativistic effects in the absence of collisions [9]. The excited states will either be the 2^3P_2 state or 3^3P_2 state depending on the light used to excite the transition. The closest electronic level to the 2^3P_2 state is the 2^3P_1 state which is 2.29 GHz higher in frequency. The closest electronic level to the 3^3P_2 state is the 3^3P_1 state which is 0.659 GHz higher in frequency. The light is chosen to be close enough to the respective transition frequency as to not couple with these other states making the system resemble the general two level system discussed next.

1.2 The Two Level Atom

The purpose of Section (1.1) is to show that, under a certain set of approximations, the Schrödinger equation can be solved for the atomic wave functions of Helium. Up to this point, the discussion has been limited to trying to describe the ground state and has not mentioned methods for to solving for higher excited states. Methods for doing this exist in the literature [7], but of more interest to this research is what happens when the Helium atom is in a laser light field. If the radiation spectrum is narrow enough to couple only two levels in the atom as in Figure (1.2), then only two electronic levels need to be considered as other levels have negligible effects. This is called the two level atom approximation.

Consider the time dependent Schrödinger equation as in Eq. (1.1), with a laser light field coupling two levels. The Hamiltonian $\mathcal{H}$ can be expressed

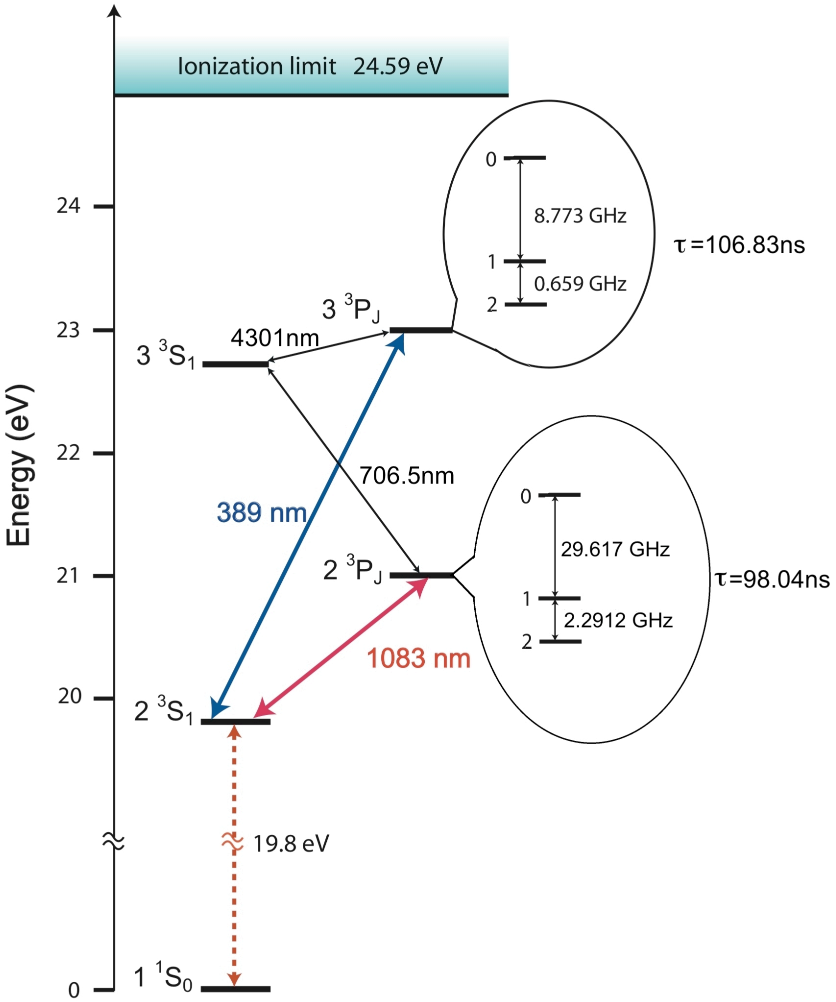

Figure 1.1: A diagram describing the revelant electronic energy levels in Helium.

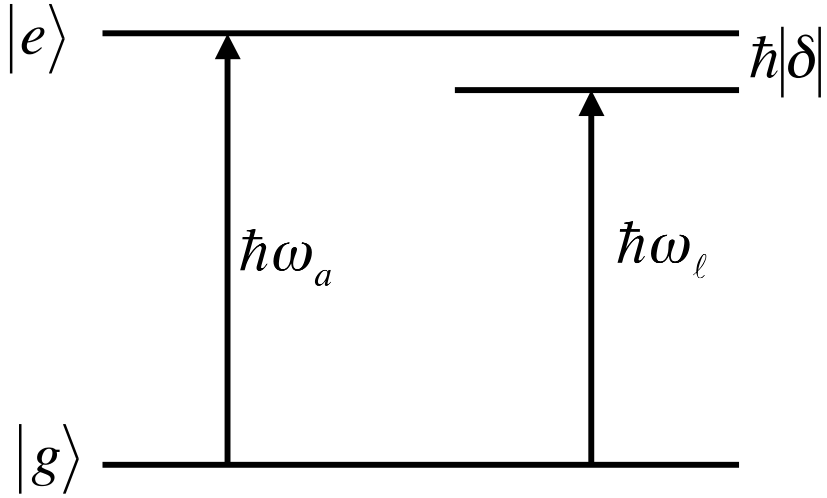

Figure 1.2: Simplified energy levels of the two level atom. The ground $|g\rangle$ and excited $|e\rangle$ states are separated by $\hbar\omega_a$. Laser light couples the two states, and can be detuned from the atomic resonance by $\delta \equiv \omega_\ell - \omega_a$.

as a time independent, field free term, $\mathcal{H}_0$, and a term with time and field dependence, $\mathcal{H}'(t)$ [10]. $\mathcal{H}_0$ has energy eigenvalues of $E_n \equiv \hbar\omega_n$ and spatial eigenfunctions of $\phi_n(\vec{r})$. So as not to confuse the two level atom's spatial wave function with the spatial wave function of the bare Helium atom, ϕ will be used instead of ψ. Since the $\phi_n(\vec{r})$ are orthogonal and form a complete set, $\Psi(\vec{r},t)$ can be expanded as

$$\Psi(\vec{r},t) = \sum_k c_k(t)\phi_k(\vec{r})e^{-i\omega_k t} \tag{1.11}$$

Using this expansion and the separating the Hamiltonian into its two parts yields

$$(i\hbar)\left(\frac{\partial}{\partial t}\right)\sum_k c_k(t)\phi_k(\vec{r})e^{-i\omega_k t} = \left[\mathcal{H}_0 + \mathcal{H}'(t)\right]\sum_k c_k(t)\phi_k(\vec{r})e^{-i\omega_k t} \tag{1.12}$$

Taking the time derivative of the left side of Eq. (1.12), multiplying both sides of the equation by $\phi_j^*(\vec{r})$, and integrating over the spatial coordinates gives

$$i\hbar\frac{dc_j(t)}{dt} = \sum_k c_k(t)\mathcal{H}'_{jk}(t)e^{i\omega_{jk}t} \tag{1.13}$$

where $\mathcal{H}'_{jk}(t) \equiv < \phi_j|\mathcal{H}'(t)|\phi_k >$ and $\omega_{jk} \equiv (\omega_j - \omega_k)$. This is merely rewriting the Schrödinger equation in a different form; no approximations have been made.

Truncating the differential equation, Eq. (1.13), to two terms describes an atom that has only two levels, a ground and excited state. This approximation is to say that the laser field only couples these two levels and all other levels act as perturbations to the system. Labeling the ground state to be $1 \rightarrow g$ and the excited state as $2 \rightarrow e$ gives

$$\begin{aligned} i\hbar\frac{dc_g(t)}{dt} &= c_e(t)\mathcal{H}'_{ge}(t)e^{-i\omega_a t} \\ i\hbar\frac{dc_e(t)}{dt} &= c_g(t)\mathcal{H}'_{eg}(t)e^{i\omega_a t} \end{aligned} \tag{1.14}$$

where $\omega_a = \omega_{jk}$ is the frequency between the two coupled levels as defined by Figure (1.2).

1.2.1 Rabi Oscillations

Equations (1.14) define the time dependence of the wave function of a two level atom. To describe the two level atom in a laser light field the momentum in the field free Hamiltonian $\mathcal{H}(t) = \frac{p^2}{2m}$ can be replaced by the canonical momentum $p \rightarrow p + (e/c)\vec{A}(\vec{r},t)$, where $\vec{A}(\vec{r},t)$ is the vector potential of the laser light.

The resulting Hamiltonian can be split into two parts, a time independent $\mathcal{H}_0 = \frac{p^2}{2m} + V$ and a time dependent Hamiltonian

$$\mathcal{H}'_{ge} = -e\vec{\mathcal{E}}(\vec{r}, t) \cdot \vec{r} = -\vec{d} \cdot \vec{\mathcal{E}} \tag{1.15}$$

where terms of $\vec{A}^2(\vec{r}, t)$ are ignored, $\vec{\mathcal{E}} = \frac{\dot{\vec{A}}}{c}$ has been defined as the electric field that couples the levels, and the electric dipole approximation has been made. Obtaining this time dependent Hamiltonian is well documented in [10, 11].

If the laser light coupling the levels of the atom is traveling in the $+z$ direction, with frequency ω_ℓ and an electric field given by $\mathcal{E}(\vec{r}, t) = \mathcal{E}_0 \hat{x} \cos(kz - \omega_\ell t)$, then the time dependent Hamiltonian becomes $\mathcal{H}'_{ge} = \hbar\Omega \cos(kz - \omega_\ell t)$ where

$$\Omega \equiv -\frac{e}{\hbar}\mathcal{E}_0 < e|\vec{r} \cdot \hat{x}|g > \tag{1.16}$$

is called the Rabi frequency.

Decoupling Eqs. (1.14), defining $\Omega' \equiv \sqrt{\Omega^2 + \delta^2}$ with $\delta \equiv \omega_\ell - \omega_a$ and taking the rotating wave approximation to drop higher order terms gives

$$c_g(t) = \left(\cos\frac{\Omega' t}{2} - i\frac{\delta}{\Omega'} \sin\frac{\Omega' t}{2} \right) e^{i\delta t/2} \tag{1.17}$$

$$c_e(t) = -i\frac{\Omega}{\Omega'} \sin\frac{\Omega' t}{2} e^{-i\delta t/2} \tag{1.18}$$

with the initial conditions that $c_g(0) = 1$ and $c_e(0) = 0$.

By plotting the square of Eq. (1.18), the population of the atoms in the excited state can be seen, as in Figure (1.3). For $\delta = 0$, each interval of $\Omega t = \pi$ transfers the atom from the ground/excited state to the excited/ground and

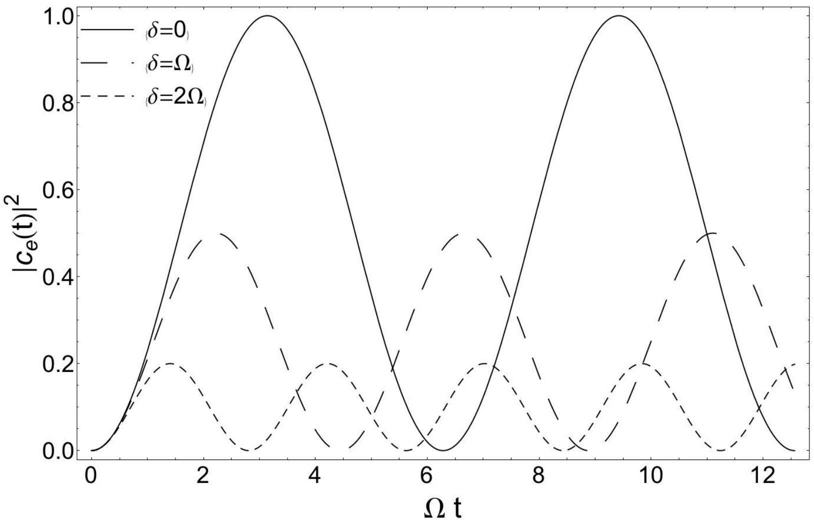

Figure 1.3: As can be seen by the curves, when the laser is detuned away from resonance full population inversion no longer occurs and the oscillation period gets shorter.

is called a π-pulse.

1.2.2 Optical Bloch Equations

The density matrix formalism can be used to describe the two level system and will lead into a discussion of the Optical Bloch Equations. The density matrix for the two-level atom expressed in the previously defined variables is

$$\rho = \begin{pmatrix} c_g c_g^* & c_g c_e^* \\ c_e c_g^* & c_e c_e^* \end{pmatrix} = \begin{pmatrix} \rho_{gg} & \rho_{ge} \\ \rho_{eg} & \rho_{ee} \end{pmatrix} \tag{1.19}$$

where $\rho_{ee} = c_e c_e^*$ gives the probability for the atom to be in the excited state. Transforming into a rotating frame and combining the components to form three real parameters gives [12]

$$u = c_g c_e^* + c_g^* c_e \tag{1.20}$$

$$v = i(c_g c_e^* - c_g^* c_e) \tag{1.21}$$

$$w = |c_e|^2 - |c_g|^2 \tag{1.22}$$

$$\vec{R} = (u, v, w).$$

By defining $\hbar\vec{\Omega} = (\mathrm{Re}(\mathcal{H}'_{ge}), \mathrm{Im}(\mathcal{H}'_{ge}), \hbar\delta)$ the time dependence of the Bloch vector, $\vec{R}$, can be written as

$$\frac{d\vec{R}}{dt} = \vec{\Omega} \times \vec{R}. \tag{1.23}$$

The methodology of arriving at the Optical Bloch Equations from the density matrix is well documented [10, 11, 13, 14] and will not be presented here. For reference, the Optical Bloch Equations for a two-level atom are

$$\begin{aligned}
\frac{d\rho_{gg}}{dt} &= +\gamma\rho_{ee} + \frac{i}{2}\left(\Omega^*\tilde{\rho}_{eg} - \Omega\tilde{\rho}_{ge}\right)\\
\frac{d\rho_{ee}}{dt} &= -\gamma\rho_{ee} + \frac{i}{2}\left(\Omega\tilde{\rho}_{ge} - \Omega^*\tilde{\rho}_{eg}\right)\\
\frac{d\tilde{\rho}_{ge}}{dt} &= -\left(\frac{\gamma}{2} + i\delta\right)\tilde{\rho}_{ge} + \frac{i}{2}\Omega^*\left(\rho_{ee} - \rho_{gg}\right)\\
\frac{d\tilde{\rho}_{ge}}{dt} &= -\left(\frac{\gamma}{2} - i\delta\right)\tilde{\rho}_{ge} + \frac{i}{2}\Omega\left(\rho_{gg} - \rho_{ee}\right)
\end{aligned} \tag{1.24}$$

where $\tilde{\rho}_{ge} \equiv \rho_{ge} e^{-i\delta t}$, $\tilde{\rho}_{eg} \equiv \rho_{eg} e^{i\delta t}$, and the spontaneous emission rate has been defined as [15]

$$\gamma = \frac{\omega_a^3 d^2}{3\pi\epsilon_0 \hbar c^3} \tag{1.25}$$

where d is the electric dipole moment defined as $\mathcal{H}'_{ge}$ in Eq. (1.15). The lifetime of the excited state is then $\tau = 1/\gamma$.

The Optical Bloch Equations account for all of our major experimental parameters and can be solved for the steady state [10]:

$$\rho_{gg} - \rho_{ee} = \frac{1}{1+s} \tag{1.26}$$

$$\rho_{eg} = \frac{i\Omega}{2(\gamma/2 - i\delta)(1+s)} \tag{1.27}$$

where

$$s \equiv \frac{|\Omega|^2/2}{\delta^2 + \gamma^2/4} \equiv \frac{s_0}{1 + (2\delta/\gamma)^2} \tag{1.28}$$

and the on resonance saturation parameter is

$$s_0 = 2|\Omega|^2/\gamma^2 = I/I_s. \tag{1.29}$$

In Eq. (1.29), the saturation intensity can also be written as $I_s = \pi hc/3\lambda^3\tau$.

Chapter 2

Optical Forces on Atoms

Now that the two level atom in a radiation field has been discussed, this chapter will serve to give a short introduction to the forces that light can apply to two-level atoms.

2.1 Radiative Force

A two level atom in a traveling wave laser light field has a significant probability of absorbing light if the separation of the atom's electronic levels corresponds to the frequency of the incoming light. Upon absorption of the light, the atom will receive momentum $p = h/\lambda = \hbar k$ in the direction of the incoming light and will be in the excited state. After absorption, the atom can return to the ground state by spontaneous emission. The spontaneous emission will be symmetric, and over a large number of spontaneous emissions the net momentum change of the atom will average to zero, as seen in Figure (2.1). When considering a large number of absorption/spontaneous emission cycles, the momentum

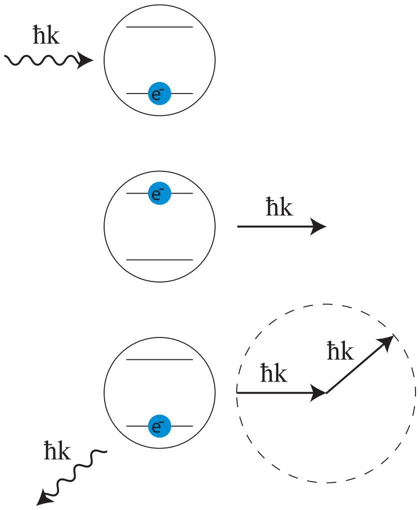

Figure 2.1: This diagram shows the radiative force process. In the first step, light impinges on an atom. In the second step, that atom absorbs the light and receives momentum of $\hbar$k. In the third step, the atom spontaneously emits in a random direction.

does not average to zero in the direction of the incoming light resulting in the radiative force.

Since the radiative force is due to the net momentum gain from the absorption of the incoming light, the force can be written as

$$F = \hbar k \gamma \rho_{ee} \tag{2.1}$$

where γ and ρ_{ee} are defined in the previous chapter. The equation is made up of three parts: $\hbar k$ which is the momentum gained by the atom per absorption, γ which is the rate at which the atom decays from the excited state, and ρ_{ee} which is the probability for the atom to be in the excited state [10]. For s $\ll$

1,

$$\rho_{ee} = \frac{s}{2(1+s)} = \frac{s_0/2}{1+s_0+(2\delta/\gamma)^2} \tag{2.2}$$

and the radiative force becomes

$$F_{rad} = \hbar k \gamma_p = \frac{\hbar k s_0 \gamma/2}{1+s_0+(2\delta/\gamma)^2}. \tag{2.3}$$

As the intensity of the light is increased, the force approaches a maximum value of F$_{rad,max} = \hbar k\gamma/2$.

2.2 Optical Molasses

A two level atom in a standing wave radiation field created by counter propagating two laser beams is another well studied system. Doppler optical molasses occurs for light tuned near the atomic transition frequency and of low intensity, and will be discussed first. High intensity optical molasses occurs when the light intensity is larger (s $\gg$ 1) and the frequency of the light is no longer as close to the atomic transition frequency and will be discussed second.

For an atom in a low intensity light field, the total scattering rate is low and stimulated emission can be ignored. Atoms in a standing wave see the sum of a radiative force coming from each direction. For atoms moving with velocity, v, the Doppler shift, $\pm kv$, is added to the detuning of the laser frequency in Eq. (2.3). Adding the two opposing radiative forces from counter propagating beams given by Eq. (2.3) gives

$$
\begin{aligned}
F_{DM} = F_1 + F_2 &= \frac{\hbar k s_0 \gamma/2}{1 + s_0 + [2(\delta - kv)/\gamma]^2} - \frac{\hbar k s_0 \gamma/2}{1 + s_0 + [2(\delta + kv)/\gamma]^2} \\
&\approx \frac{8\hbar k^2 \delta s_0 v}{\gamma(1 + s_0 + (2\delta/\gamma)^2)^2}.
\end{aligned} \tag{2.4}
$$

Figure (2.2) shows the force versus velocity in this case of Doppler optical molasses, and it appears the force would quickly bring the atoms to zero velocity if there were no outside influences. However, there is competition between the heating effects from the discrete nature of each momentum step and the damping from the force that result in a nonzero kinetic energy in a steady state.

In the limit where $s \gg 1$, the force can no longer be considered the superposition of two radiative forces because stimulated emission, multi-photon processes, and nonlinear effects can occur. The optical force due to a high intensity standing wave was calculated using the density matrix formalism [16] and was followed by Minogin and Serimaa's paper [17] where the problem is solved by a continued fraction approach. These two papers give the details of high intensity optical molasses.

From these papers, a Mathematica script was written by Allred [4] and shows the force versus velocity curves for different detunings and powers. The results from these calculations can be seen in Figure (2.3).

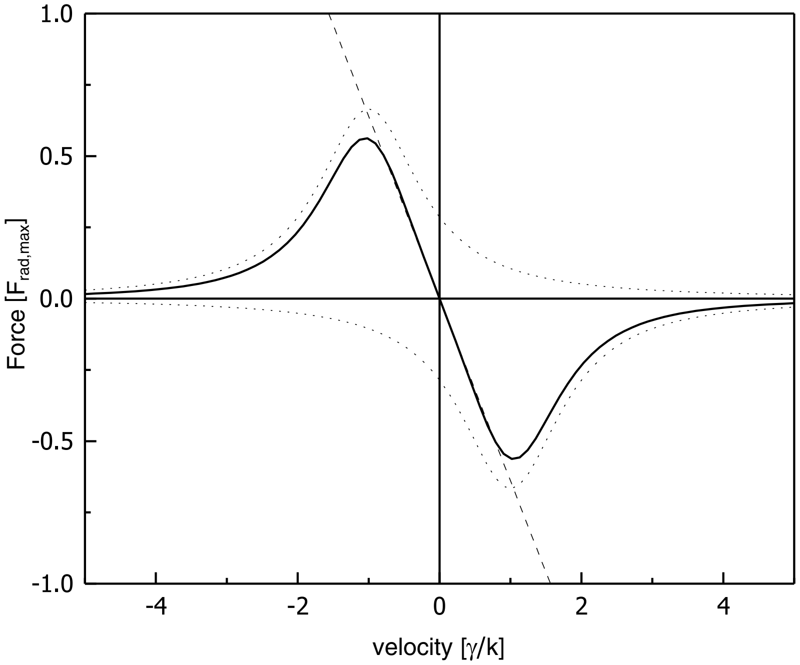

Figure 2.2: In the low intensity limit, the process of absorbtion followed by spontaneous emission in a standing light wave gives a force profile as seen above. The vertical axis is in units of $\mathrm{F}_{rad,max} = \hbar k\gamma/2$. In a range of $\approx \pm\gamma/k$ the atom sees a force that opposes its motion. At zero velocity, the atom feels no force.

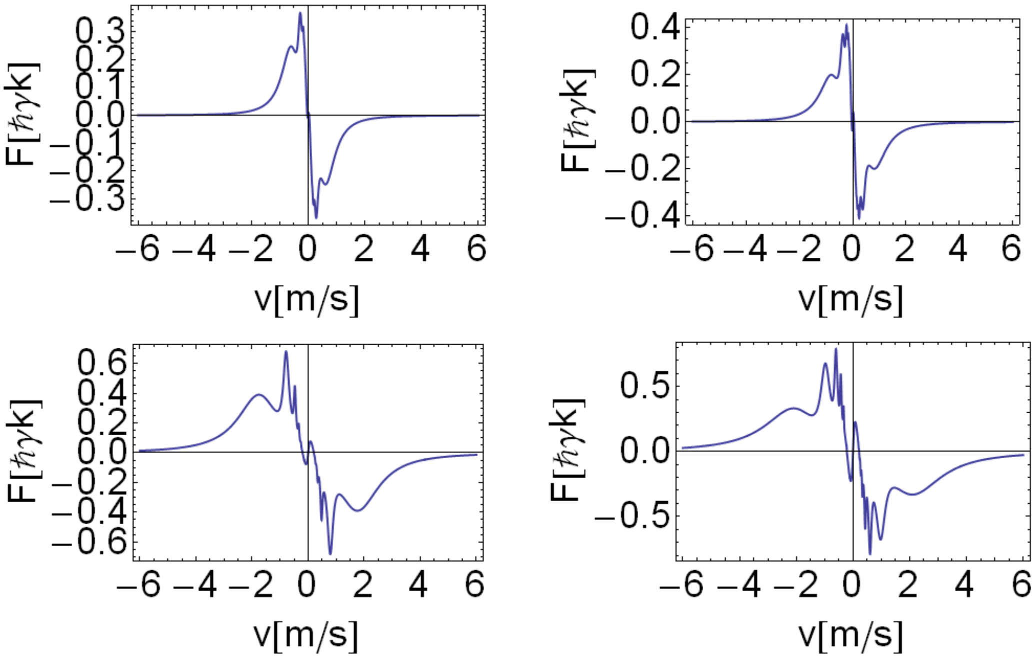

Figure 2.3: High intensity optical molasses force versus velocity profiles for (a) $\delta = -1.2\gamma$, $s_0 = 10$, (b) $\delta = -1.2\gamma$, $s_0 = 20$, (c)$\delta = -5\gamma$, $s_0 = 50$, (d) $\delta = -5\gamma$, $s_0 = 100$. It can be seen for high intensities near zero velocity the force reverses directions.

2.3 Bichromatic Force

The force caused by laser light with two frequencies is well studied in previous theses in our lab [4, 18–21]. The bichromatic force is used as a tool to collimate our atomic beam, and yet still has interesting theoretical problems to be solved [22]. A short description will be given of the special properties that the use of bichromatic light fields creates.

Consider two counter-propagating beams in the $\pm z$ directions each with two frequencies, $\omega \pm \delta$ with $\delta \ll \omega$ but $\delta \gg \gamma$. If the two beams have a relative phase difference of ϕ, then the total electric field is given by

$$\mathcal{E} = 2\mathcal{E}_0 \Big[\cos(\omega t - kz)\cos\big(\delta t - \frac{\phi}{4}\big) + \cos(\omega t + kz)\cos\big(\delta t + \frac{\phi}{4}\big) \Big]. \tag{2.5}$$

This equation shows that there will be an envelope frequency that is slow (δ) and a carrier frequency (ω) which is fast as seen in Figure (2.4). If the carrier frequency is set to the atomic transition frequency and the envelope is chosen such that during the time between nodes, one pulse, satisfies the π-pulse condition, then in a time of π/δ the two level atom will change its state. The atom can be driven to the excited state by a pulse coming from the one direction and then de-excited by stimulated emission from a pulse coming from the other direction. Each absorption or spontaneous emission imparts momentum $p = \hbar\mathrm{k}$ in the same direction to the atom, and repeats every π/δ so that the maximum force is

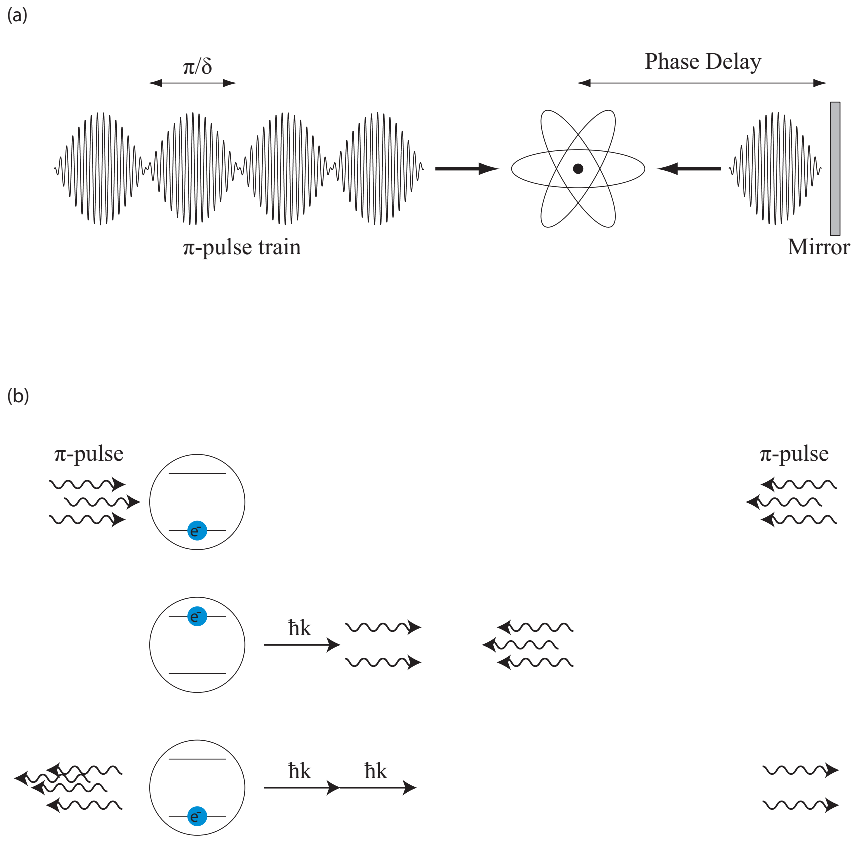

Figure 2.4: The two frequencies in the bichromatic laser beam create a series of π-pulses from the beat frequency. Each π-pulse excites or de-excites the atom in a time of π/δ leading to a force $(\hbar k\delta/\pi)$ much larger than $F_{rad,max}$.

$$F_b = \frac{\Delta p}{\Delta t} = \frac{2\hbar k}{\pi/\delta} = \frac{2\hbar k\delta}{\pi}. \tag{2.6}$$

This is much larger than $F_{rad,max}$ $\hbar k\gamma/2$ since $\delta \gg \gamma$

The Optical Bloch Equations for the light field of Eq. (2.5) can be numerically integrated to solve this bichromatic force problem. When tested numerically, and accounting for spontaneous emission, it is found that $\phi \approx \pi/2$ in Eq. (2.5) gives the largest force as shown in Figure (2.5) from [21].

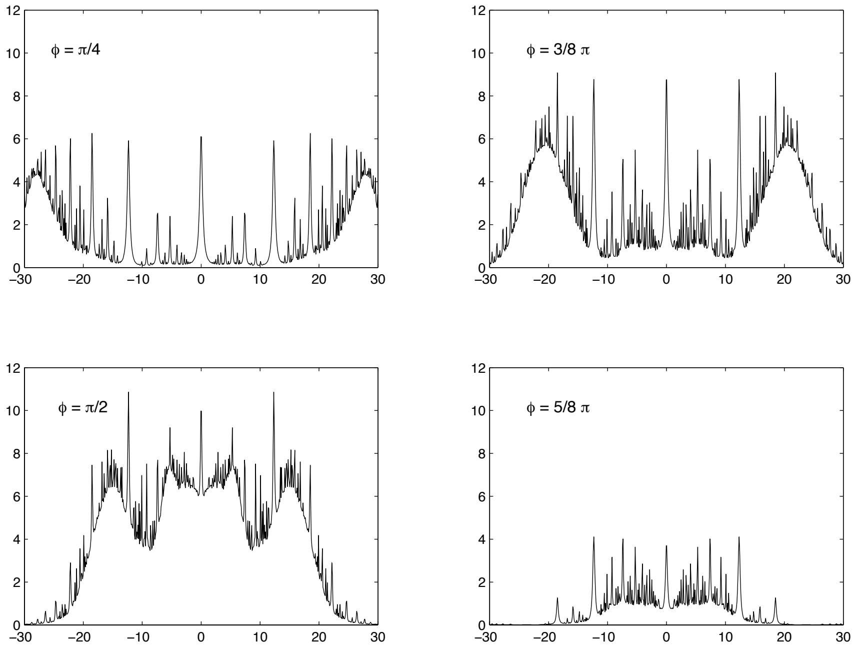

Figure 2.5: Numerically calculated force in units of $(\hbar k\gamma)$ versus velocity in units of (γ/k) curves for different relative phases. The spikes are partly numerical artifacts and partly multiphoton processes. In these plots, the Rabi frequency is $\Omega = 41\gamma$ and the detuning is $\delta = 37\gamma$ to match experimental parameters.

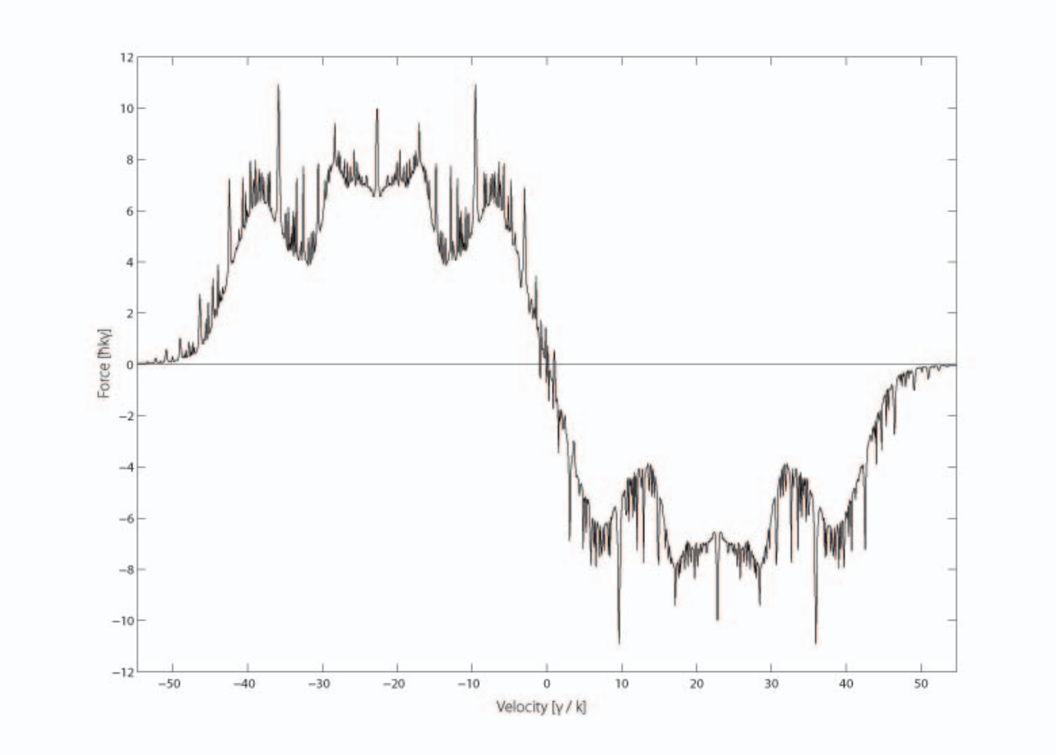

Figure 2.6: Numerically calculated force of the bichromatic collimation with $\delta = 37\gamma$, $\Omega = 41\gamma$, $\phi = \frac{\pi}{2}$ from [21].

Figure (2.5) shows the bichromatic force centered about zero velocity. To use this force to collimate the atomic beam, the laser frequencies are shifted by $\pm\delta/2k$. These four frequencies shift the resulting profile to be centered around a non-zero velocity. The resulting force is unidirectional so that collimation requires two regions for each dimension, making four bichromatic force regions to collimate our atomic beam [23]. Figure (2.6) shows the velocity dependence of the bichromatic force in one dimension as used to collimate the atomic beam.

2.4 Dipole Force

The dipole force is the last force to be discussed because in this experiment it is used for patterning of the atomic beam while the other forces are used for collimating the atomic beam.

In an electromagnetic field, the ground state energy level of this two level system is shifted by approximately

$$\Delta E_g \sim \frac{\hbar\Omega^2}{4\delta} \tag{2.7}$$

for $\delta \gg \Omega$ as in [10, 11]. In a single frequency standing wave light field, the energy levels are spatially modulated because there is a spatial variation of intensity in the light field. The dipole force is proportional to the gradient of this light shift and so

$$F_{\mathrm{dip}} = -\nabla(\Delta E_g). \tag{2.8}$$

If an intensity of $I(z) = I_0 \cos^2(kz)$ is used as the intensity of the standing wave and $\Omega = \gamma\sqrt{\frac{I(z)}{2I_s}}$ is used as defined at the end of Chapter 1, then

$$F_{\mathrm{dip}} = \frac{\hbar k \gamma^2 I_0}{8\delta I_s} \sin(2kz). \tag{2.9}$$

The force can be made large because it does not saturate at high optical intensities. It is also proportional to the gradient of the optical field intensity and modulates on the wavelength scale. This experiment will take advantage of the wavelength scale of this force to pattern an atomic beam.

Chapter 3

Laser Systems

To create a bright, collimated He* beam using the optical forces described in the previous chapter, light of the appropriate wavelength must be produced. For this experiment, light for the collimation of the He* atoms acts on the $2^3S_1 - 2^3P_2$ transition at $\lambda = 1083.33$ nm. This wavelength is available from commercial diode lasers. The first part of this chapter will describe the tailoring and amplification of the light used for the collimation of the He* beam.

The optical mask, which is described in Chapter 5, patterns the He* beam after collimation. Experiments have been performed on this $2^3S_1 - 2^3P_2$ transition at $\lambda = 1083.33$ nm and on the $2^3S_1 - 3^3P_2$ transition at $\lambda = 388.98$ nm. The infrared light for the optical mask is again provided by a commercially available diode. The ultra-violet light is produced by frequency doubling a Titanium-Sapphire laser. The second part of this chapter will describe the production and tailoring of the two optical masks.

3.1 1083.33 nm Collimation Light System

The laser light at $\lambda = 1083.33$ nm used for collimation is provided by a Spectra Diode Labs (SDL) model SDL-6702-H1 distributed Bragg reflector (DBR) diode laser assembly packaged in an 8 pin TO-3 window mount. The assembly includes a thermistor and thermoelectric cooler, and has a wavelength tuning rate of +0.084 nm/°C [18]. The output of the diode has a spectral line width of about 3 MHz and must be narrowed to under the 1.6 MHz natural line width of the $2^3S_1 - 2^3P_2$ transition. This is done with an extended cavity, as seen in Figure (3.1), consisting of a $70\% - 30\%$ beam splitter and retro-reflecting mirror. The cavity length is controlled by a piezo-electric transducer (PZT) that the mirror is mounted on. With this set-up, the laser line width is narrowed to approximately 125 kHz [18].

For shielding against temperature drifts and air currents, the extended cavity set-up is placed on a 305 mm x 710 mm x 76 mm Aluminum slab and inside a box constructed of polystyrene foam insulation. The temperature inside the box is stable to better than 0.5°C/hr, but will have long term temperature drifts that follow the laboratory conditions over the day. An ILX Lightwave LDT-5910 temperature controller keeps the diode at 23.9 ± 0.1°C.

The current control for this collimation diode is provided by a Thorlabs LDC 500. The diode current determines both the frequency and output power of the diode as can be seen in Figure (3.2) and Figure (3.3). In Figure (3.2), the diode output power was measured by a Newport 1825-C power meter with an 818-SL detector. In Figure (3.3) the frequency was measured using a Burleigh WA-1500 wave meter after the diode light had been coupled into a single mode

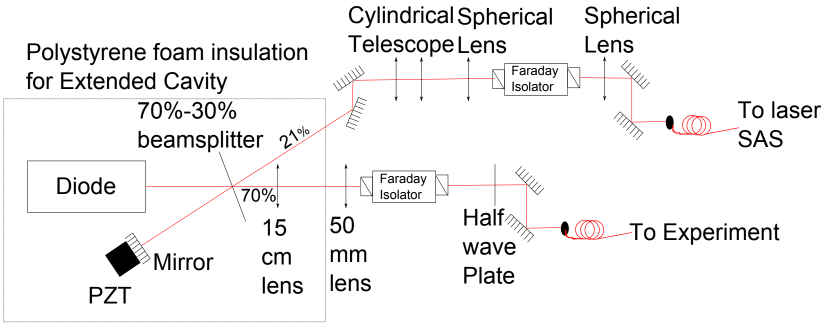

Figure 3.1: Schematic of the extended cavity diode laser set-up. A portion of the light is reflected back into the DBR to narrow the line width from 3 MHz to 125 kHz. The beam divergence out of the laser is compensated by lenses so that the light passes through all the optical elements.

fiber. It should be noted that these figures vary slightly from previous figures [21] as the diode temperature set point was changed from 24.1°C to 23.9°C to account for differences in laboratory temperature and humidity conditions.

The main (70%) output beam from the extended cavity goes through a set of cylindrical lenses to shape the beam allowing it to pass through an OFR IO-3-1083-HP optical isolator. The light then passes through a half-wave plate and is coupled into a single mode optical fiber. The optical fiber gives a nice Gaussian mode laser beam at the output and isolates the extended cavity set-up from the rest of the system.

The leakage output beam (21% because of the one reflection and one transmission through the beam splitter) is shaped by a cylindrical telescope and then focused by a spherical lens through an OFR IO-D-1080-Z optical isolator. A spherical lens, after the isolator, is used to focus the light so that it can be coupled into an optical fiber.

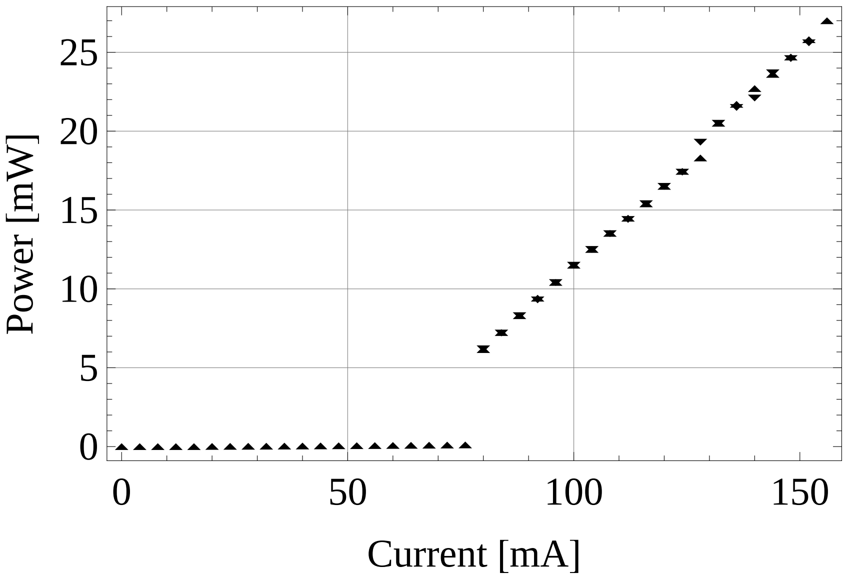

Figure 3.2: Plot of output power versus drive current of the diode laser used for optical collimation at 23.9±0.1°C. Triangles pointing upward indicate increasing the drive current, while downward pointing triangles indicate decreasing the drive current.

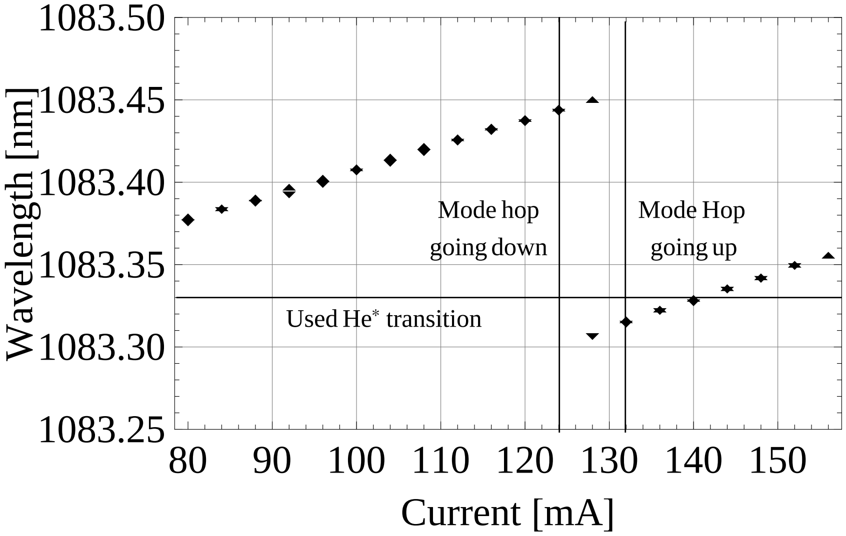

Figure 3.3: Plot of the wavelength versus drive current of the diode laser used for collimation at 23.9 ± 0.1°C. As in the preceeding figure, triangles pointing upward (downward) indicate increasing (decreasing) drive current.

3.1.1 Four Frequency production

After the extended cavity described in the previous section, the light enters a region where four frequencies are produced for the bichromatic collimation as described in Chapter 2. The four frequencies needed to collimate the atomic beam using the bichromatic force are $\omega_a \pm \delta + kv$ and $\omega_a \pm \delta - kv$, where ω_a corresponds to the $2^3S_1 - 2^3P_2$ transition frequency in He*.

The four frequencies are produced by double passing an acousto-optic modulator (AOM) as described first in experiments with Rubidium [24]. Figure (3.4) shows the set-up where the main and first deflected beams are retro-reflected to create two beams with spectral components (ω_ℓ, $\omega_\ell + 2\delta$) and ($\omega_\ell + \delta$, $\omega_\ell - \delta$) respectively. The AOM, driven by a Mini-Circuits ZOS-75+ voltage controlled oscillator (VCO) amplified by a MiniCircuits ZHL-1-2W RF amplifier, defines $\delta = 2\pi \times 60$ MHz.

The total power in each two frequency beam after double passing the AOM is ~1 mW and must be amplified to get the numerically calculated optimal intensity of $\sim 4000 s_0$ [19, 21, 24]. It is also important for the two frequencies in each beam have the same relative intensity. To this extent, polarization maintaining optical fibers are used to transport the two beams to either Fabry-Perot interferometers or fiber amplifiers. This flexibility allows the frequencies in each beam to be balanced by tilting the AOM and monitored using the Fabry-Perot interferometers while maintaining the polarization into the fiber amplifiers after each move.

Each dual-frequency beam seeds a Keyopsys Ytterbium (Yb)-doped fiber amplifier, models KPS-BTQ-YFA-NLS-1083-40-COL. The fiber amplifiers work

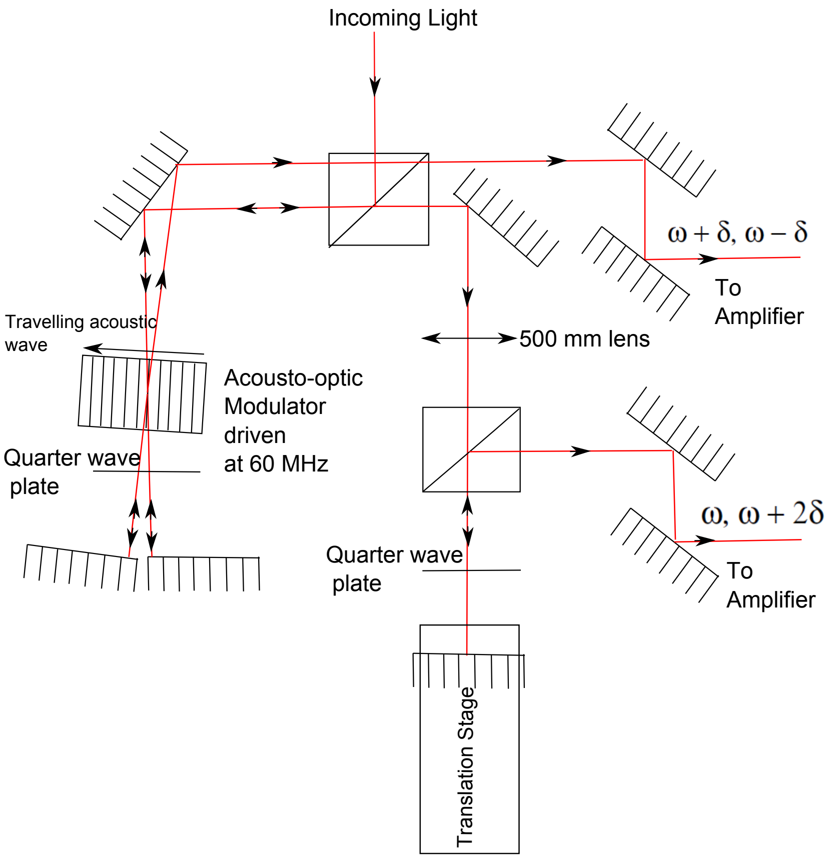

Figure 3.4: The four frequencies for bichromatic collimation are produced by double passing an AOM as seen above. The translation stage provides a way to tune the relative phase difference between the envelope phase of the $\omega_a \pm \delta + kv$ and $\omega_a \pm \delta - kv$ beams.

by using commercially available high power 977 nm diode lasers to pump the outer fiber cladding, injected through a V-groove of the Yb-doped fiber to invert the population inside the fiber. A small amount of seed light can then initiate stimulated emission and amplification. The fiber amplifiers begin with a pre-amp stage that saturates the input for the next two amplification stages. This helps the final output power to be less dependent on the seed power, while providing (without further) amplification approximately 100 mW at the output. The first power amplification stage has a diode pump laser that can be powered by up to 5 Amperes so that the fiber provides up to 3 W of output power. The final amplification stage allows for up to 4.3 W of output power. Typically only the pre-amp stage and first amplification stage are used because the experiment only needs about ∼1 W from each amplifier to run efficiently.

Each fiber amplifier output is sent to optical collimation set-ups where the beams are shaped and split for different uses. Since the fiber amplifiers maintain polarization, polarizing beam splitter cubes following each fiber output separates the light into vertically and horizontally polarized beams. This allows the power in each beam to be changed by rotating the polarization of the fiber amplifier output and also sets the orthogonal polarization between the two bichromatic beams.

Figure (3.5) shows a schematic for the current optical collimation set-up. The $\omega_a \pm \delta + kv$ beam power is set to 650 mW of horizontally polarized light with a minimum amount of light in the vertical polarization allowing the fiber amplifier to be run with the pump and first amplification stage current of ∼2600 mA. The $\omega_a \pm \delta - kv$ has 650 mW of vertically polarized light and ∼100 mW of horizontally polarized light allowing the fiber amplifier to be

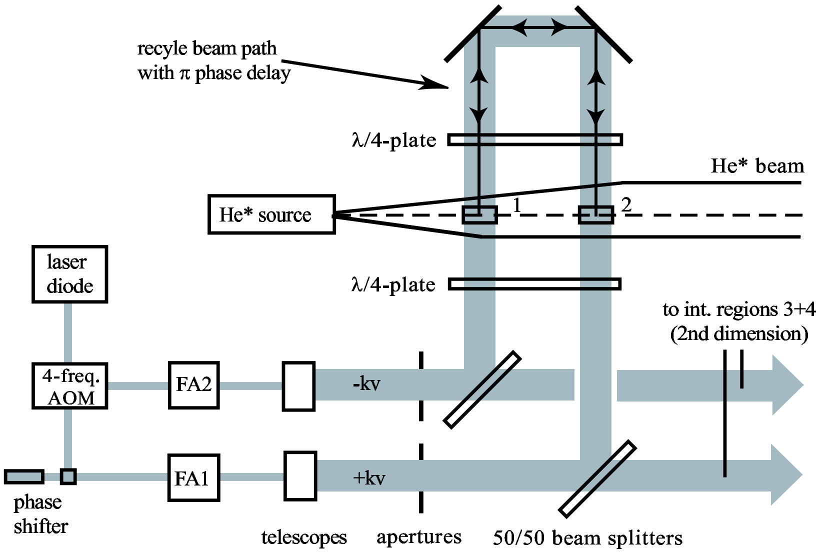

Figure 3.5: A schematic of the light beam path after the fiber amplifiers to the atomic beam.

run with the pump and the first amplification stage current of ∼3600 mA. Each 650 mW beam ($\omega_a \pm \delta \pm kv$) is collimated using spherical and cylindrical telescopes so that the final beam profiles are similar for intensity matching purposes. The waist of the elliptical beams are set to be 5.85 mm by 1.82 mm and then cut by apertures set to 10 mm in diameter to create a quasi "top hat" intensity profile.

The ∼100 mW of light from the vertically polarized $\omega_a \pm \delta - kv$ beam serves four purposes: a high intensity optical molasses, a Doppler-like optical molasses, a true Doppler optical molasses, and light for the saturation absorption spectroscopy (SAS) lock. The light is sent through the three AOMs set at 89 MHz, 81 MHz and 90 MHz taking the first deflected beam from each. The +90 MHz offset beam is coupled into an optical fiber and sent to the SAS cell to frequency lock the laser. The details of the SAS will be discussed in the next section. Since the laser frequency is locked 90 MHz above the $2^3S_1 - 2^3P_2$ transition, the 81 MHz AOM provides light tuned 9 MHz ($\sim 5\gamma$) below the atomic transition and is used to make the high intensity molasses. The light that is produced from the 89 MHz AOM is $\sim$ 1 MHz below the atomic transition and serves as the light for a Doppler-like and Doppler molasses.

After the collimation light is produced, it is sent to the vacuum system and aligned to the He* beam. The bichromatic collimation immediately following the He* source output has an atom transverse velocity capture range of ±40 m/s and collimates to a transverse velocity spread of about ±9 m/s [19]. This is followed by a high intensity optical molasses with a velocity capture range of ±9 m/s and collimates atoms to about ±3 m/s. The capture range of a Doppler optical molasses is $v_c = \gamma/k \sim 1.7$ m/s for $\gamma/(2\pi) = 1.62$ MHz and $\lambda = 1083.33$, which means that a Doppler optical molasses would not capture many of the ±3 m/s atoms after the high intensity molasses. If the intensity of a Dopper-like molasses is a few times the transition's saturation intensity, a rough estimate using the power-broadened line width of the transition, $\gamma' = \gamma\sqrt{1+s_0}$, to calculate a power broadened velocity capture range of ∼3 m/s. Therefore, a Doppler-like optical molasses is used to collimate the atoms to under $\pm v_c$. Since the Doppler-like molasses has so much intensity, it became useful to split off 125 μW to make a Doppler optical molasses of the correct intensity. The Doppler optical molasses is used to collimate the atoms in the patterning dimension to about ±1 m/s and to steer the atoms.

3.1.2 Saturation Absorption Spectroscopy Locking

Saturation absorption spectroscopy (SAS) can be used to lock the laser frequency to the $2^3S_1 - 2^3P_2$ transition by using the leakage light from the extended cavity set-up and a He* source. A glass cell, filled with Helium, wrapped with coils of wire driven at 52 MHz by an HP 8640, and amplified by an EIN 440 LA RF operates a discharge to provide the He* atoms. The radio frequency interacts with the Helium in the cell and causes a discharge and the resulting collisions transfer some small fraction of the Helium to the He* state.

SAS requires three laser beams: a pump, a reference, and a probe. As seen in Figure (3.6), the probe and reference beams pass through the cell of He* and the pump beam is set to counter-propagate with the probe beam. The reference and probe beams are created using the two reflections from the two surfaces of a thick piece of glass. The stronger pump beam is taken from the transmission through the thick piece of glass and counter-propagates the pump beam as shown in Figure (3.6). The probe and reference beams pass through the cell and are reflected on to photodiodes wired to subtract their photocurrents.

When the laser frequency is tuned through atomic resonance in the absence of the pump beam, as in (a) of Figure (3.7), both the probe and reference experience a decrease in intensity as the atoms absorb the resonance light, and the width of the absorption signal is due to the Doppler effect. If the strong pump beam is present it will also interact with the atoms but with opposite Doppler shift and excite on resonance atoms. The counter propagating probe

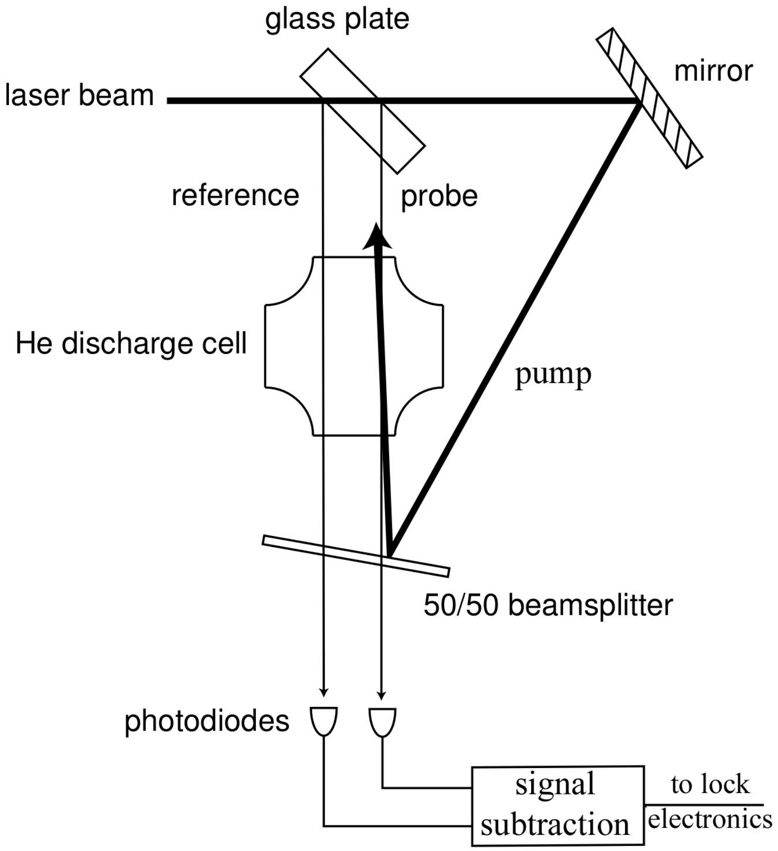

Figure 3.6: A schematic of saturation absorption spectroscopy used for frequency locking a laser.

beam will interact with the same atoms as the probe beam only if both Doppler shifts are zero so there will be less probe absorption near the atomic transition frequency as the pump beam has already excited some of the atoms. The increase in transmission intensity near resonance is called the Lamb dip and is much narrower than Doppler width as seen in (b) of Figure (3.7). By using the reference beam, the Doppler broadened signal can be subtracted from the probe signal leaving only the Lamb dip shown as a peak in Figure (3.8) where the laser frequency is swept slowly through resonance.

The Doppler free signal in the middle trace of Figure (3.8) is centered at the frequency to which the laser can be locked. To keep the laser at the center of Lamb dip, the frequency of the laser is changed by a small amount by dithering the diode current. The dithering produces an ac component allowing a lock-in detector to demodulate the SAS signal to a DC error signal shown as a dispersion shape in the bottom trace of Figure (3.8). The error signal then controls the PZT on the back of the extended cavity mirror.

To implement this lock, the diode current is modulated with a 10 kHz sine wave signal that is provided by a Stanford Research Systems (SRS) D345 30 MHz synthesized function generator along with a ten turn 100 kΩ resistor, which allows the dither current amplitude ($\sim 10^{-6}$ amps corresponding to $\sim$1 MHz) to the diode to be adjusted. The sine wave is also used as a reference for the EG&G Princeton Applied Research model 5104 lock-in amplifier. The SAS signal with the diode current dithered is sent to a Stanford Research Systems (SRS) SR560 low-noise preamplifier that filters out the noise below 3 Hz and above 30 kHz to provide the input for the lock-in amplifier. The DC error signal from the output of the lock-in amplifier is then sent to an SRS SIM960

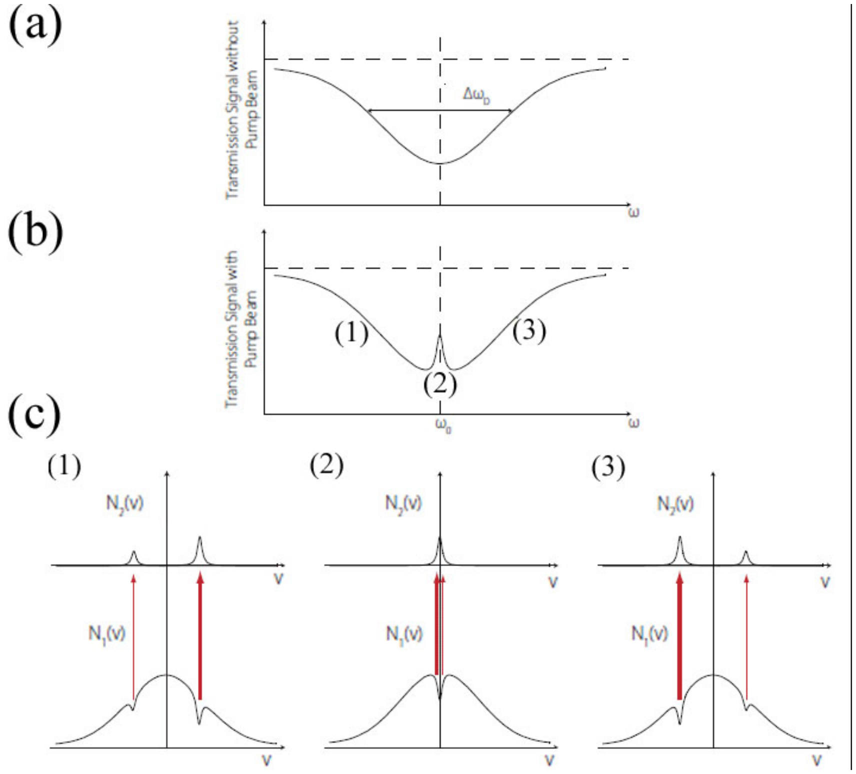

Figure 3.7: (a)The absorption of light due to the Doppler-broadened width of the the atoms. (b)The absorption of the the probe beam in the presence of the pump beam. Note the appearance of the Lamb Dip. (c) The excitation of different velocity classes by the pump and probe beam are shown in (1), (2) and (3). The Lamb dip occurs when the two beam excitations overlap at v=0 as in (2).

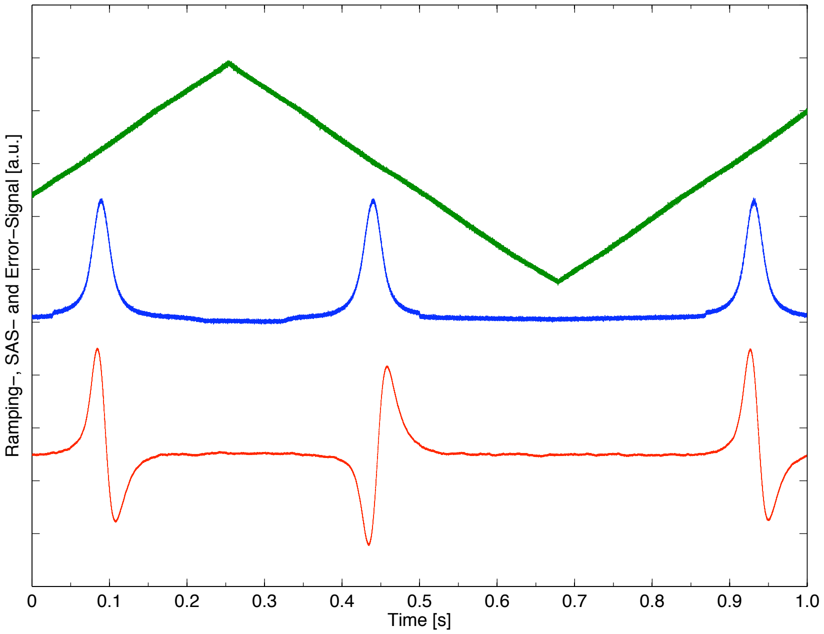

Figure 3.8: By driving the PZT on the back of the extended cavity mirror with a triangle wave (top line), the laser frequency can be swept through atomic resonance. Usually the triangle wave is set to 30 Hz, but is slowed here to 1 Hz to get a better picture from the oscilloscope. The middle line is the subtracted signal from the SAS photodiodes, and the inverted Lamb dip can be clearly seen. The bottom line is the error signal used for frequency locking feedback produced from the SAS signal.

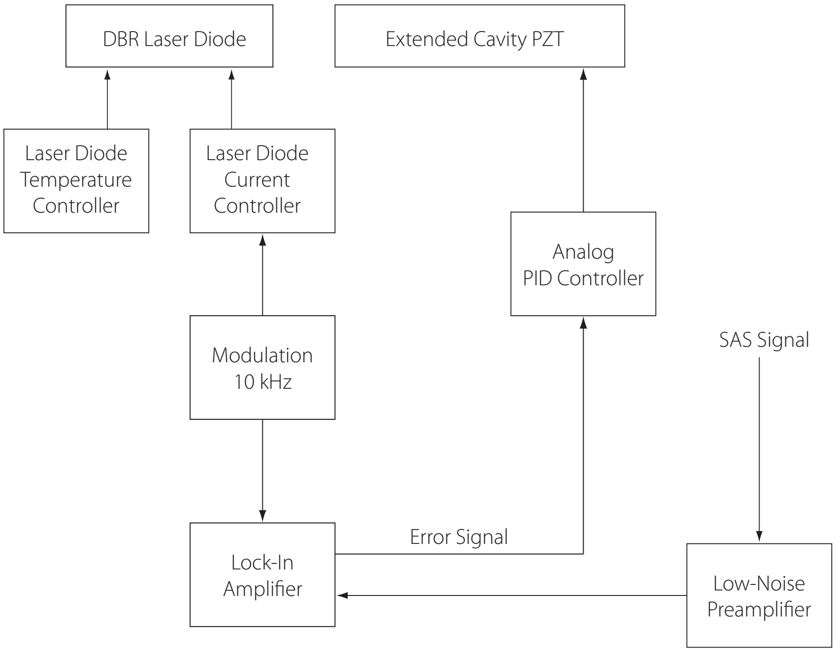

Figure 3.9: A block diagram showing the arrangement of the electronics used to frequency lock the laser.

analog PID controller. After the PID controller, the signal is sent through low pass filters and voltage amplifiers to prepare the signal for feedback to the PZT in the extended cavity. Figure (3.9) shows a block diagram of the electronics described above. Using this set-up, under normal operating conditions, the laser can stay locked on the order of hours.

3.2 1083.33 nm Optical Mask System

The laser light at 1083.33 nm used for the optical mask is provided by a separate Spectra Diode Labs (SDL) model SDL-6702-H1 distributed Bragg reflector (DBR) diode packaged in an 8 pin TO-3 window mount. This optical mask diode laser has an extended cavity much like the collimation diode laser, and also sits on the aluminum slab in the polystyrene foam box, as seen in Figure (3.1), to provide temperature stability. A Newport model 325 temperature controller maintains the optical mask diode laser at a constant temperature by measuring the resistance of a thermistor that is currently kept at 9.73 kΩ which corresponds to about 24°C. The diode laser current is supplied by a Newport 505 laser diode driver.

To prevent back reflections into this extended cavity set-up, an OFR IO-3-1083-HP optical isolator is used in the main beam. Both beams are eventually coupled into single mode optical fibers for experimental ease, where the main beam is used for the optical mask and the leakage beam for SAS frequency locking. As before, spherical and cylindrical telescopes are used to shape both beams for coupling.

After the single mode optical fiber, the main beam is focused by an f = 75 mm spherical lens onto a small aperture Brimrose AOM to produce a beam tuned 490 MHz above the $2^3S_1 - 2^3P_2$ transition. A HP3200B RF generator operating near its maximum frequency provided the 490 MHz driving signal for the AOM until it was replaced by a Minicircuits ZOS-765+ VCO operating in the middle of its frequency range. Regardless of the RF source, a Minicircuits ZHL-1-2W RF amplifier produces the $\sim$1 W of power needed to drive the AOM. A 50 mm lens is used to focus the first deflected beam so that it can be coupled into an optical fiber, fed through ThorLabs FPC030 polarization paddles which are described in [21]. The light is amplified by a Optocom Innovation OIYb30 1W variable Yb-doped fiber amplifier.

For stability purposes, the output coupler of the amplifier is placed on a breadboard attached to the vacuum system, so that the movement of the laser beam due to vibrations is coupled to the movement of the vacuum system. The light power is maximized through a polarizing beam splitter cube by using the optical fiber polarization paddles. The light is then circularly polarized by a quarter wave plate which allows the retro-reflected beam to be monitored during an experimental exposure. The light goes through a spherical lens (to focus the light at the sample) and a cylindrical telescope before finally arriving in front of the sample. The final waists of the elliptical beam are approximately 0.40 (horizontal) x 1.60 (vertical) mm.

The laser is frequency locked to $2^3S_1 - 2^3P_2$ transition using a SAS set-up similar to the one described in the previous section. Although the electronics diagram is the same for both set-ups, different equipment is used. A Princeton Applied Research model 126 lock-in amplifier is used to produce both the 10 kHz sine wave to dither the diode current and the error signal. The lock also uses an analog SRS SIM960 PID controller to help keep the lock stable up to several hours.

3.3 388.98 nm Light Production

The optical mask using the $2^3S_1 - 3^3P_2$ transition in He* comes from a Titanium-Sapphire (Ti-Sapph) laser that is frequency doubled to produce the necessary light, since diode lasers of suitable power are not currently available at this wavelength. Much of the workings of this system has been described nicely in S.H. Lee's Ph.D. thesis [25], but a short review of the frequency locking mechanisms and changes will be discussed below. The systems can be split into two basic parts: 1) Red light at 777.95 nm is made via a Ti-Sapph laser with a Pound-Drever-Hall frequency lock to control short term drifts and a SAS frequency lock to control long term drifts. 2) A frequency doubling cavity from Coherent is used to make the 388.98 nm light from the Ti-Sapph output.

3.3.1 Ti-Sapphire Laser

To create light at 388.98 nm, frequency stable light near 777.95 nm must first be produced. A Ti-Sapph laser is a good choice for producing light at this wavelength because it falls in the middle of the gain curve for the laser's crystal, and it is capable of producing a few Watts of power.

A Coherent Verdi V10 diode laser pumps an SEO Schwartz Titan-CW series Ti-Sapph with 9 W of 532 nm light. The mirrors inside the Ti-Sapph's bowtie cavity are specified to have a range of 700-820 nm which are able to produce a TEM_{00} output beam that has a divergence on the order of 1 mrad. With 9 W of pumping light, the Ti-Sapph usually produces around 2.2 W at 777.95 nm.

3.3.2 Pound-Drever-Hall Lock

The Ti-Sapph laser frequency is stabilized to a Fabry-Perot cavity by means of a Pound-Drever-Hall (PDH) locking system. This method of locking is described in other places and only a brief review of will be given here [25, 26].

The output of the Ti-Sapph laser is split into four beams: one that carries most of the power which seeds a frequency doubling cavity and three low power

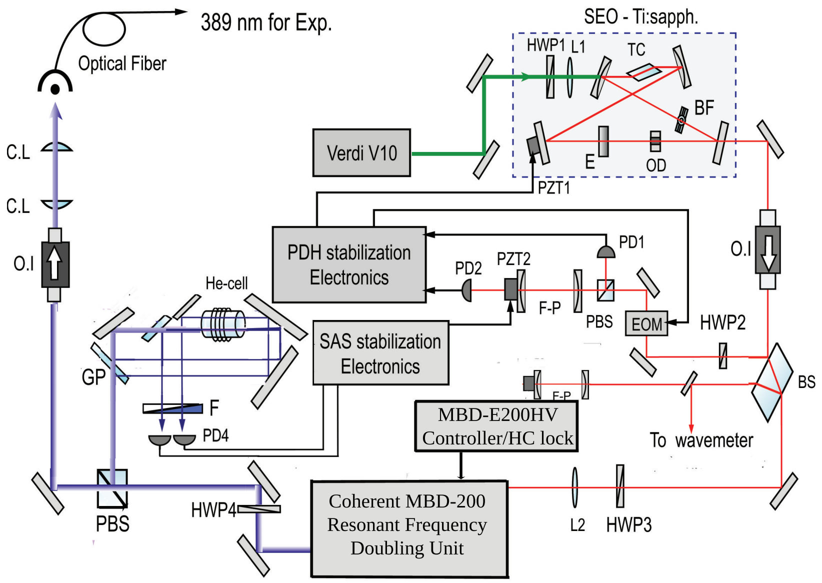

Figure 3.10: A schematic for the production of light at 388.98 nm.

beams as can be seen in Figure (3.10). The first low power beam is sent to a Burleigh WA-1500 wave meter to coarsely monitor the frequency to ±50 MHz. The second low power beam is used to generate the PDH lock error signal. The third low power beam is sent to a reference Fabry-Perot interferometer (F-P II in the figure) and is used to monitor the optical mode structure of the Ti-Sapph cavity.

The light used for the PDH lock is given frequency sidebands at $\omega_\ell \pm \omega_{pdh} = \omega_\ell \pm 60$ MHz from an electro-optical modulator driven by an HP3200B with a Mini-Circuits ZHL-1-2W amplifier. Then the light is passed through a beam splitter cube to a Fabry-Perot cavity. The reflection off the front face of the Fabry-Perot travels back to the beam splitter where the deflected light is focused on a photodiode. The photodiode signal is zero when the Fabry-Perot cavity is on resonance because both sidebands reflect back with equal amplitudes and π phase difference. When the cavity is not on resonance, the amplitudes of the reflected sidebands are no longer equal and a non-zero photodiode signal is produced.

The photodiode signal is amplified by Mini-Circuits ZFL500LN amplifiers and is mixed in 2 Mini-Circuits ZEM2B with the EOM driving RF. An Ortec phase shifter is used in conjunction with a Mini-Circuits ZSC-2-1 power splitter after the HP3200B and before the mixer to compensate for the phase shift between the EOM driving frequency and the photodiode signal. When tuned properly, the low frequency component is just a DC shift and can be used for an error signal by passing through a low pass filter. The passive transmission of the Fabry-Perot and the error signal produced by the filtered signal can be seen in Figure (3.11).

The signal then goes to a low noise pre-amplifier and gain control after which the signal is split into two parts. Part of the signal goes through two integral stages, amplified and then summed with the other part which passes through a proportional stage before being sent to the piezoelectric transducer on the back of one of the Ti-Sapph cavity mirrors. A schematic of the locking system can be seen in Figure (3.12), which has been taken directly from S.H. Lee's thesis [25].

3.3.3 SAS Locking

Saturation absorption spectroscopy has been previously discussed for the lock of the 1083.33 nm diode lasers. Although the SAS locking uses $\lambda = 388.98$ nm light, the lock will be discussed here because the error signal feeds back

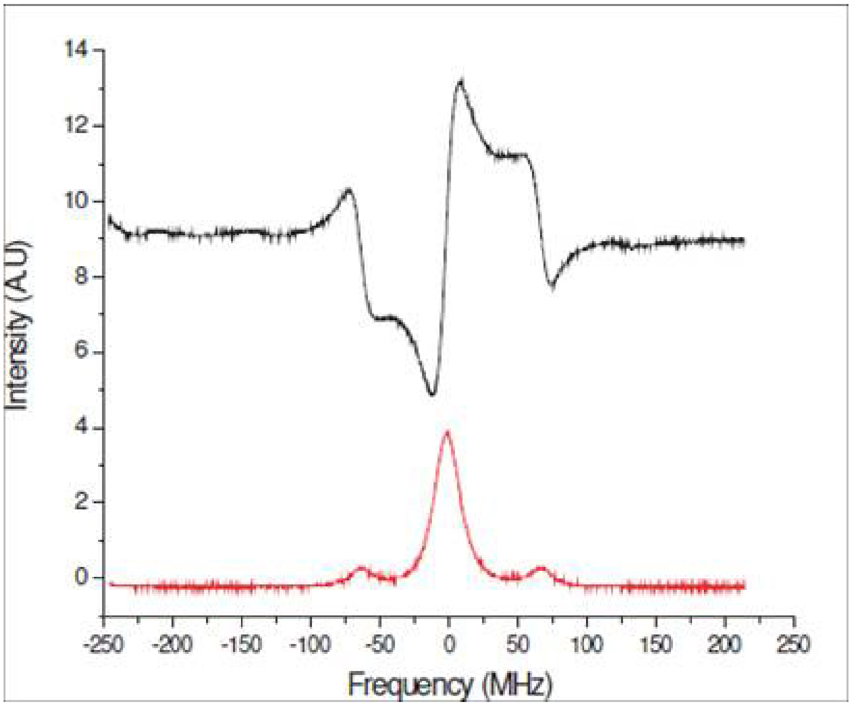

Figure 3.11: The top trace is the error signal created from the light reflected from the Fabry Perot in the PDH set-up. The bottom trace is the tranmission signal from a photodiode after the Fabry-Perot. This graph can be found in Ref. [25].

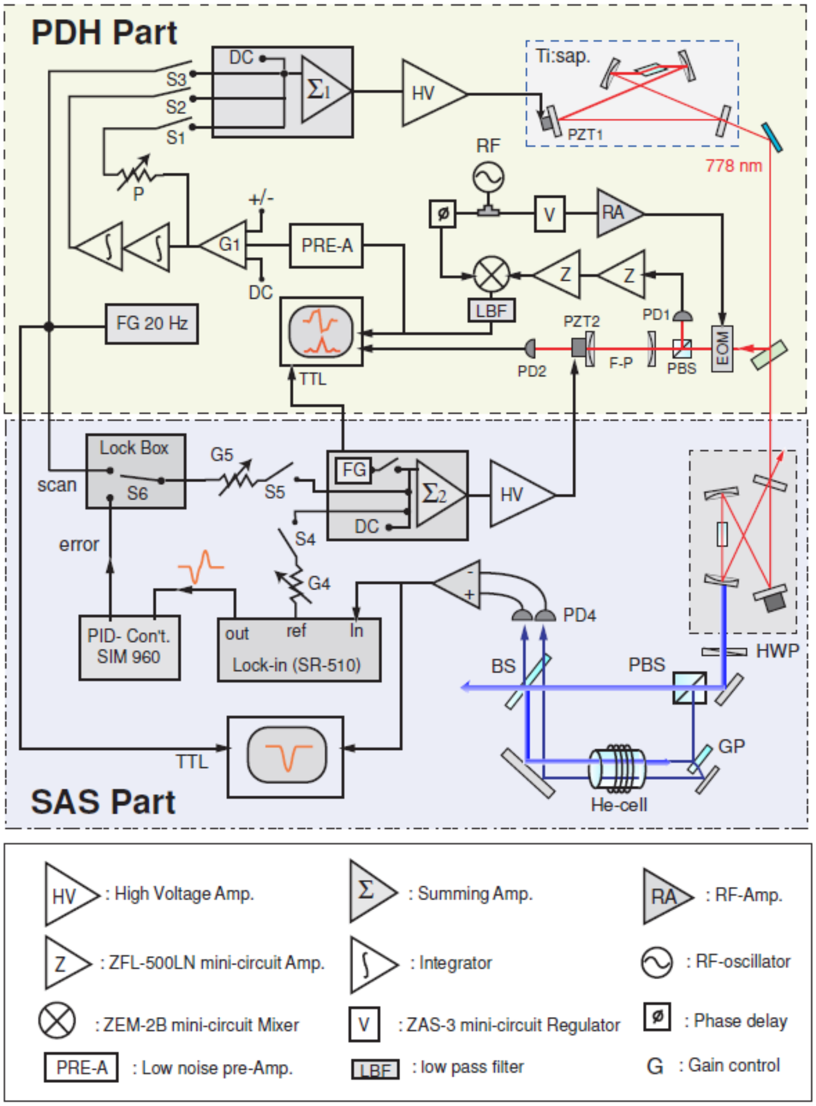

Figure 3.12: An overview of the locking electronics for the Ti-Sapph laser taken from S.H. Lee's thesis [25].

to the Ti-Sapph Fabry-Perot interferometer to stabilize it against long term frequency drifts of the system.

The pump/probe set-up is the same as before and can be seen in Figure (3.10). The cell discharge is driven by an HP3200B at 57 MHz that is amplified by a RF Power Labs Inc model FK 250-10C wideband RF Amplifier. Previously, with the diodes it was possible to dither the current of the laser, while with this system it is the Fabry-Perot cavity used for the PDH lock that is dithered at 800 Hz by a Model 124A EG & G Lock-In Amplifier. Since the laser frequency is locked to this cavity the dither is transferred to the laser frequency and is maintained through the frequency doubling process. The subtracted photodiode signal is sent to an SRS Model SR510 lock in detector with the 800 Hz signal as a reference. The error signal out of the lock-in goes to an SRS model SIM 960 PID controller and then the signal is sent to the Fabry-Perot cavity PZT. Together, the PDH and SAS locking keep the Ti-Sapph laser frequency at half the atomic resonance frequency, and has a frequency drift much less than 1 MHz. Figure (3.13) is a previously measured SAS signal [25].

3.3.4 Coherent MBD

The Coherent MBD-200 is a commercially purchased frequency doubling cavity which has been engineered to be very efficient and stable against small fluctuations in the lab environment. The optical set-up is shown in Figure (3.14). This cavity doubles the Ti-Sapph laser frequency and gives the desired frequency of light for the optical mask and SAS set-up.

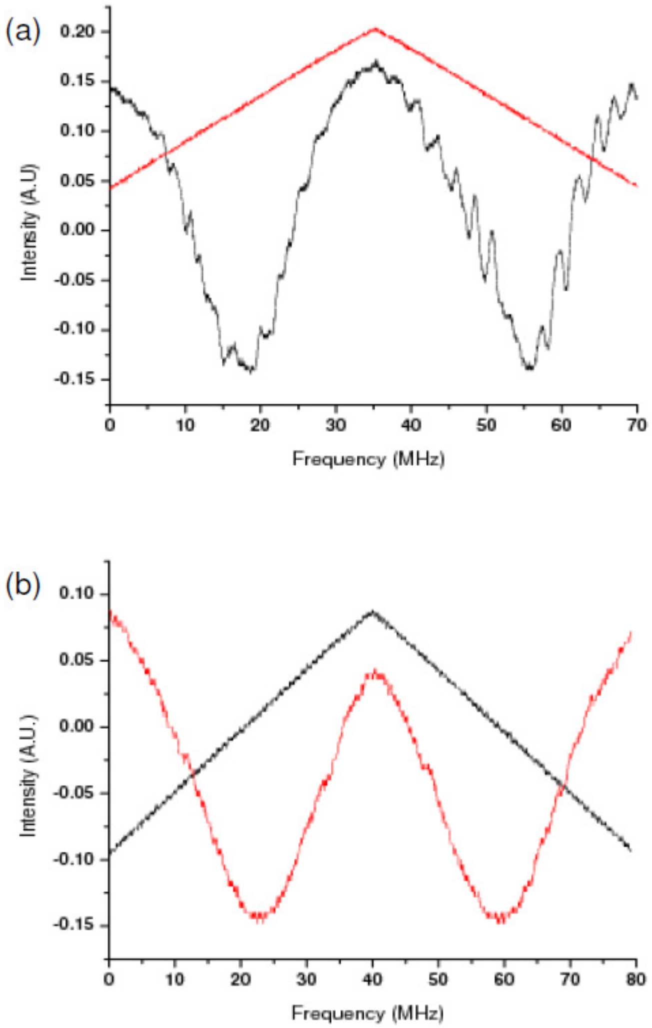

Figure 3.13: Ramp and SAS Lamb dip signal taken at a slow scan rate (≤ 1 Hz for (a) Ti-Sapph laser frequency not locked to PDH error signal and (b) Ti-Sapph laser frequency locked to PDH error signal[25].

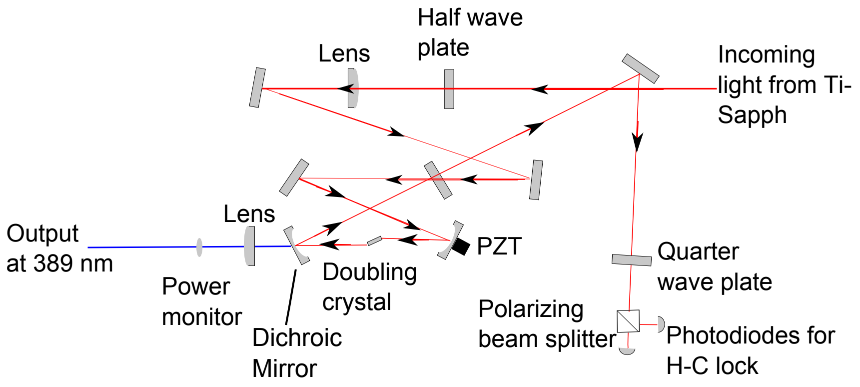

Figure 3.14: The optical path through the Coherent MBD doubling cavity

Hänsch-Coulliaud Lock

The frequency doubling cavity would not be stable without a locking system because there are various perturbations from the surrounding environment including temperature and vibrations. Hänsch and Coulliaud developed a cavity locking method based on the polarization of the incoming light. Again, this is a commonly used technique and many good references exist for further study [25, 27].

To briefly describe the technique, consider the set-up shown in Figure (3.14), where the frequency doubling cavity has low loss for horizontal polarization and higher loss for vertical polarization. If the incoming light has both vertical and horizontal polarization components, then some of the vertical polarization will reflect off the cavity input mirror and serve as a reference. After this beam goes through the quarter wave plate, it becomes circularly polarized and is split evenly by the polarizing beam splitter cube onto the photodiodes. The horizontal polarization that sees a low loss cavity will experience a frequency dependent phase shift. On each pass through the cavity, some light will come out through the input mirror and overlap with the vertically polarized light. If the cavity is on resonance, this light will have no phase shift leaving the signal on the photodiodes unchanged. However, if the cavity is slightly shorter/longer, the light in the horizontal polarization will experience a positive/negative phase shift and the quarter wave plate will create elliptically polarized light. Then the relative intensity on the two photodiodes will not be balanced, and will indicate which way the cavity moved.

Since the locking system was designed by Coherent Inc., the electronics are all hidden from the user. An MBD-E200HV electronics unit provides a clean signal for locking purposes. The error signal is made to be about 0.5 Volts peak-to-peak by changing both the quarter wave plate in the MBD-200 box and the polarization of the incoming light. Once the error signal appears as in Figure (3.15), the locking switch is turned on. Locking the cavity increases the power out of the cavity from about ∼1.5 mW passive transmission to near 500 mW when locked while being pumped with ∼1.6 Watts from the Ti-Sapph laser.

3.4 388.98 nm Optical Mask system

After making the 388.98 nm light, it is coupled into a Thorlabs 405 nm high power, polarization maintaining optical fiber after a half wave plate to align the polarization of the light along the fast axis of the fiber. A half wave plate after the fiber allows the polarization to be changed to maximize the performance of a quartz AOM driven by an Isomet VCO/Amplifier at 80 MHz. A piece of glass in the laser beam line allows the power of the light to be monitored

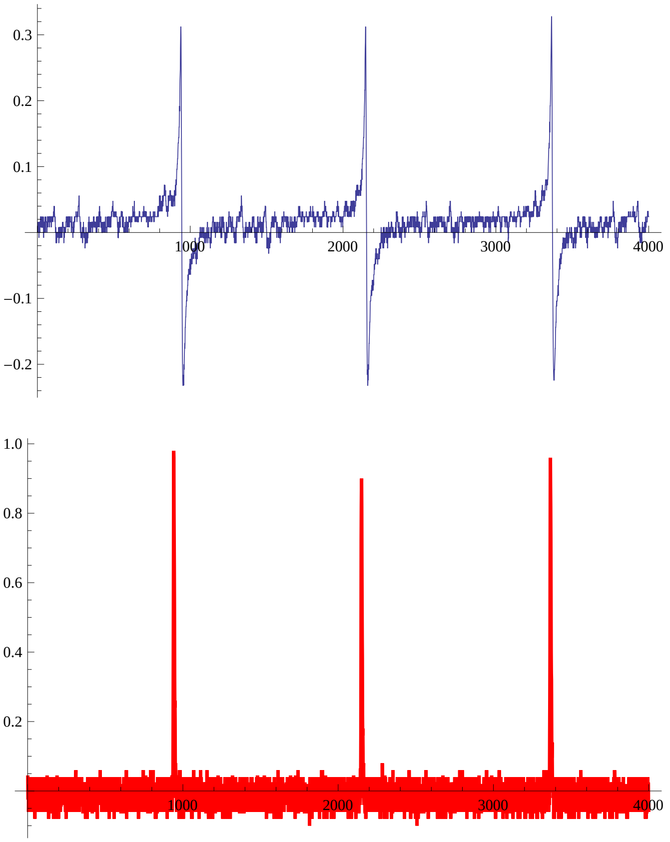

Figure 3.15: The top is a trace of the signal after the photodiode subtraction. The lower graph is the power monitor signal.

during the operation of the experiment. After the glass, there is a spherical lens and cylindrical telescope which make the beam waists 0.181 (horizontal) mm by 1.12 (vertical) mm at the sample. Although the frequency doubling cavity produces nearly 500 mW, a typical run day has about 5-15 mW of light in front of the sample due to losses with fiber coupling, AOM deflection efficiency, and uncoated lenses.

Chapter 4

Vacuum System

A bright metastable 2^3S_1 Helium (He*) beam is very advantageous for lithography as it provides short exposure times. To produce and transport He* effectively, the experiments are carried out in a high vacuum chamber, seen in Figure (4.1), that has a background vapor pressure of $\sim 10^{-7}$ Torr. The system is made mostly from 6 inch Conflat flanges with 4 inch diameter beam pipes, and is capable of reaching the ultra-high vacuum regime. However, the He* source uses KF flanges to connect the Helium gas flow, and the lithography region has O-ring sealed doors which limit the pressure even with a cold trap. Furthermore, operating requires that the lithography region be opened frequently to load and retrieve the samples, and this prevents long periods of uninterrupted pumping and leads to slightly higher pressures.

The vacuum system consists of a source and a beam-line chamber separated by a thin metal wall, located at (a) in Figure (4.1), with a 0.5 mm aperture that allows differential pumping. The source chamber is pumped by a Pfeiffer TPH 330 turbo molecular pump backed by a Pfeiffer Duo 110 mechanical pump.

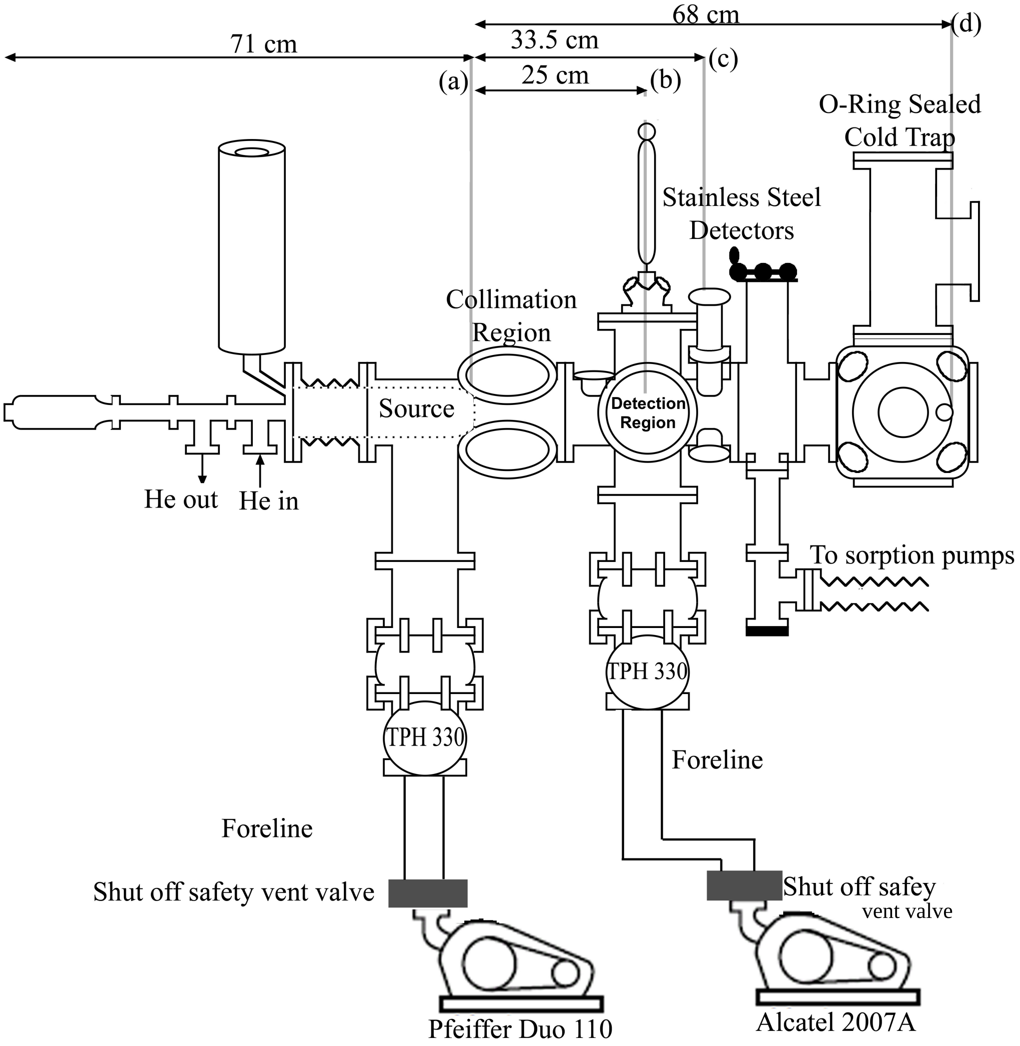

Figure 4.1: The system divides nicely into four parts: a source, a collimation, a detection and a lithography region.

The volume that it pumps is significantly smaller than that of the beam line region, but it must also handle the large influx of Helium gas when the source is running. The beam line chamber is pumped by a separate Pfeiffer TPH 330 turbo molecular pump backed by a 2007A Alcatel direct drive pump.

As in Figure (4.1), the vacuum system is protected by foreline shut-off safety vent valves between the mechanical pumps and the turbo molecular pumps that protect the system from the back streaming of oil if the electrical power is unexpectedly cut off. The Pfeiffer Duo 110 has a Pfeiffer model ONF 25 safety foreline valve, while the 2007A Alcatel pump has a Lesker auto-off safety vent valve. The valves remain open while the power is on and the pressure on the mechanical pump side is lower than the foreline pressure. When the power trips, the valves close within 30 milliseconds to prevent oil from streaming into the system after which small porous holes slowly bring the mechanical pump up to atmospheric pressure. The turbo molecular pumps also turn off and will not restart when the power comes back on. When the power returns, the mechanical pumps will start but the valves will not open because the pressure is lower in the foreline. The system will sit valved off until the proper action can be taken or the mechanical pumps bring down their pressure below foreline.

4.1 Source Chamber

The excitation of ground state Helium to He* is commonly achieved using a DC-discharge. Our source uses a reverse flow DC-discharge built at Universiteit Utrecht from the design of Kawanaka et al. [28] and modifications by

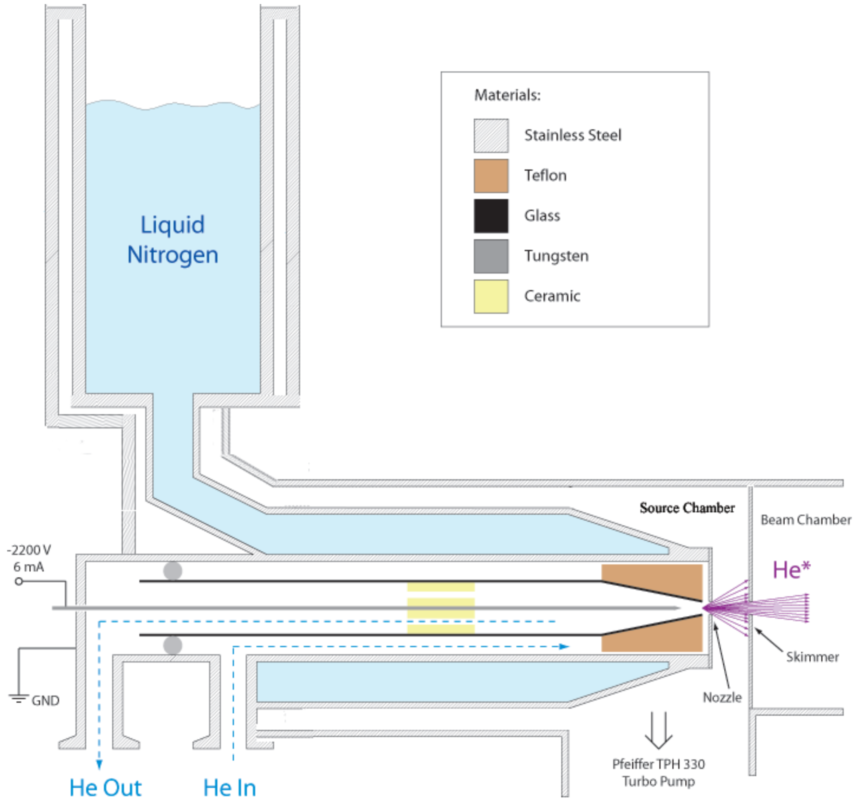

Figure 4.2: The reverse flow DC-discharge source used in the experiment as seen in both [4, 21].

Mastwijk et al. [29].

Helium enters the source chamber through the KF flanged port shown in Figure (4.2) along the outside of a 1 cm diameter glass tube housed inside of a 3 cm diameter stainless steel cylindrical cavity. The glass tube is held in place by a Teflon spacer near the nozzle and an O-ring spacer near the input of the Helium gas. The Helium gas is cooled by the liquid Nitrogen jacket as it flows toward the nozzle end and is forced around the glass tube and into contact with the Teflon spacer. A Welch 1402 mechanical vacuum pump brings the Helium gas through a small hole in the end of the glass tube and out of the system through the second KF port. At typical operating conditions, the foreline pressure is $\sim$1.20 Torr as measured by an MKS Instruments convectron gauge.

The needle inside the glass tube is made from a welding rod of pure Tungsten. The needle is sharpened using a drill to spin the Tungsten rod while a belt sander takes material off in the axial direction to form a point. The grooves due to sanding should run parallel to the longitudinal direction of the rod.

In the vacuum system the needle is centered inside of the glass tube by a piece of ceramic that has through holes to facilitate gas flow. The glass tube sits so that the needle and the 0.5 mm hole in the nozzle plate are roughly aligned. At the other end, the needle is attached to a 1 inch Huntington feed through which allows the adjustment of the separation distance between the needle and nozzle plate while the source chamber is under vacuum.

The procedure for operating the source begins with first flowing Helium gas around the glass tube. Then the liquid Nitrogen jacket is filled, cooling the Helium gas. An HP 6525A is turned up to supply a voltage of $\sim$ -2200 V to the Tungsten needle to create an electrical discharge in the gas between the needle and the nozzle plate. When the discharge occurs, current can flow from the needle to the nozzle plate which is connected to fourteen 12 KΩ high power resistors in series to ground. The source will operate with currents from 2 and 12 mA, although the current setting of 6 mA seems to maximize the reliability of the source.

The plasma emanating from the discharge can be seen through a 1.33 inch Conflat window placed directly above the region between the nozzle plate and a skimmer plate in the vacuum system. The metastable atoms are not created in the discharge, but are created during the electron recombination process. When properly lit, the source will glow a blue-ish color.

While lit, the source turbo molecular pump backing pressure reads about 160 mTorr, and the beam-line turbo molecular pump backing pressure rises from ∼4 mTorr to about ∼8 mTorr. The absolute pressure of the source chamber measured by an ion gauge is on the order of 10^{-5} Torr while the beam line operates at 10^{-6} Torr. Time of flight measurements show the He* atoms have a roughly Maxwellian distribution with a longitudinal velocity of $v_\ell \sim 1125$ m/s and a full width of ∼440 m/s [23].

4.2 Beam Line Chamber

The beam line can be described in terms of its three regions: collimation, detection, and lithography. The collimation and detection regions are directly attached, while the lithography region is separated by an O-ring sealed gate valve after the detection region at (d) in Figure (4.1). This set-up allows the lithography region to be opened for sample loading without having to vent the entire system.

4.2.1 Collimation Region

The collimation region is a six way 6 inch Conflat cross with windows on four arms that are arranged so that the arms are ±45 degrees from the vertical. The 6 inch Conflat flanges have windows that are 4 inches in diameter with an anti-reflection(AR) coating to pass both $\lambda = 1083$ nm and $\lambda = 389$ nm light very efficiently. Arranging the arms in this manner allow light to impinge on the He* atoms from each of the four arms close to the point where they emerge from the skimmer.

The collimation region has coils of wire wrapped around the vacuum system along the longitudinal axis of atomic beam travel. The coils are arranged so that 0.30 Amps supplied by a BK Precision 1660 triple output DC power supply cancels the Earth's magnetic field component along the beam.

After the coils, there is a 2.75 inch electrical feed through that is used to supply electrostatic deflection plates, which sit in between the collimation and detection region, with 1000 V. The deflection plates are used to deflect any charge particles from the atomic beam.

4.2.2 Detection Region

Aligning the bichromatic beams and the molasses beams is most easily done with a real time detection system to see how the light is interacting with the atoms. It is also advantageous to know the absolute number of He* atoms in the atomic beam after collimation. Unfortunately, two detection systems are required to gather this information. To this extent, the detection region is another six way 6 inch Conflat cross arranged such that horizontal optical access is available and the detector can be raised out of the atomic beam as seen in Figure (4.1).

MCP/Phosphor Screen

The first detection system is made of a micro-channel plate (MCP) and phosphor screen which allows for real time imaging detection of the He* atoms. The MCP/phosphor screen assembly is mounted on a Huntington 3 inch push/pull feed through which sits on top of a Kimball Physics vacuum flange multiplexer and allows the set-up to be retracted into the top part of the cross when not in use.

The MCP/phosphor screen assembly uses Kimball physics alumina (Al_2O_3) rods, C7x7 stainless steel plates with centered one inch diameter holes, springs, and retaining rings as shown in Figure (4.3a). Wires are spot welded to the stainless steel plates and connect to power supplies outside the vacuum system through 1.33 inch electrical feed throughs on the flange multiplexer. There are a total of four stainless steel plates, one on each side of the MCP and one on each side of the phosphor screen. As seen in Figure (4.3), the front plate of the MCP is held at $\sim$ -500 V, while the back plate is grounded. The front plate of the phosphor screen is held at $\sim$1500 V while the back plate is just used to hold the phosphor screen in place.

The 25 mm diameter Burle Electro-Optics MCP is comprised of an array of lead glass tubes which have a 10 micron diameter and a center to center spacing of 12 microns. Each tube is arranged to have a 12 degree bias angle to the surface such that any electron that enters will hit the semiconducting tube wall as shown in Figure(4.3b). This will produce a cascade of electrons as the walls have been treated to optimize the secondary emission characteristics of each channel and are held at a high voltage. High purity nichrome is used

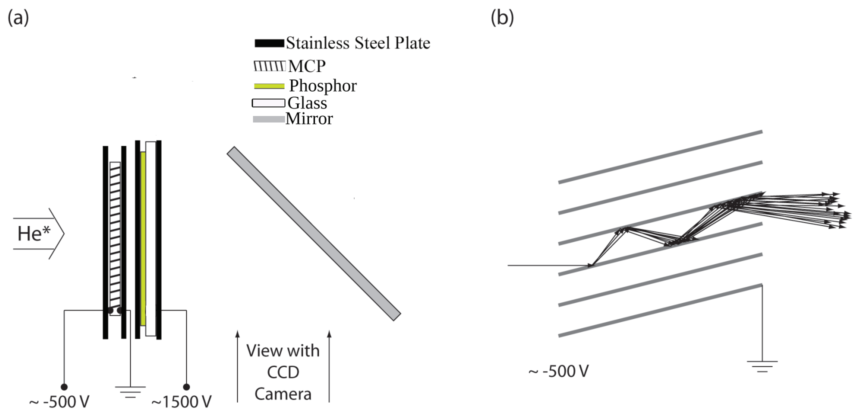

Figure 4.3: (a) Shows the MCP/phosphor screen set-up. The steel plates are held in place by Alumina rods with springs and retaining rings. The MCP and phosphor screen are held in place by pressure between the steel plates. (b) Shows the cascade of the electrons inside of the MCP

as the electrode material and there is a solid glass border. At 700 V/900 V, the typical MCP has a gain of $10^3/10^4$ as the shipping data sheets from Burle indicate. A nice review of MCPs is given by Wiza [30].

The P20 phosphor screens were originally speciality orders from Jim VanHouse. These phosphor screens have a thin layer($\sim$10 Å) of gold which provides electrical contact to the phosphor to a surrounding thicker gold ring which comes into contact with the stainless steel plates. The newer P43 phosphor screens are from Lexel Imaging and use an Indium-Tin-Oxide (ITO) coating between the glass and the phosphor to provide electrical contact to a silver ring on the outside of the phosphor which is in contact with the stainless steel plates.

A mirror at 45 degrees reflects the image of the phosphor screen toward one arm of the six way cross where a GBC model CCD-505E CCD camera captures the image. Typical images of the first and second dimensions of the

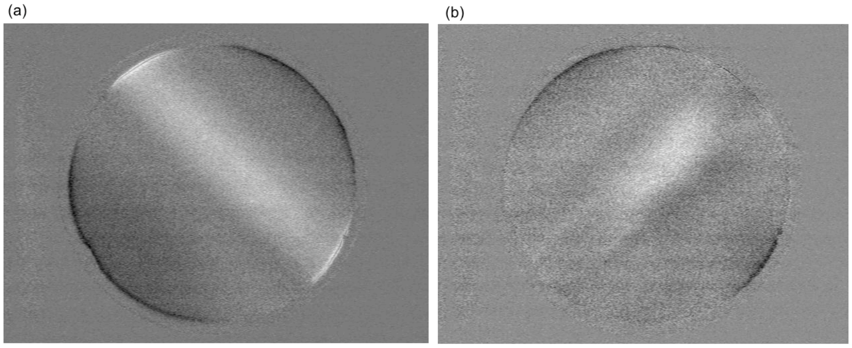

Figure 4.4: (a) Bichromatic collimation of the first dimension (b) Bichromatic collimation of the second dimension. The circle is 25.4 mm in diameter.

bichromatic collimation can be seen in Figure (4.4). The collimation is at 45 degrees from the horizontal because of the arrangement of the arms of the 6 way cross in the collimation region.

Stainless Steel Detectors

The MCP/phosphor screen allows for near real time imaging of the atomic beam, but absolute He* numbers are hard to determine since the intensity of the screen is highly non-linear. For this purpose, we use a stainless steel detector, which is a linear detector. The stainless steel detector consists of two slits that are perpendicular to each other and a back plate. The front slit and the back slit/back plate combination are each attached to separate 2 inch Huntington feed throughs that allow each slit to be moved independently. The 0.205 mm wide front slit and the 0.5 mm wide back slit form a rectangular aperture as seen in Figure (4.5) taken from Allred's thesis [4]. The He* atoms that pass through the aperture hit the stainless steel back plate and have a 70% efficiency of ejecting an electron from the surface [31]. The two slits are kept

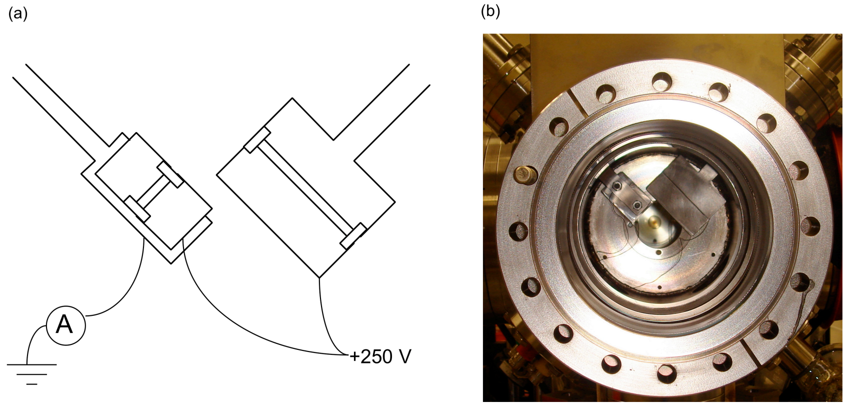

Figure 4.5: (a) Schematic of front stainless steel detectors (b) Experimental set-up of stainless steel detectors

at +250 V which accelerates the ejected electron toward the slits. The current measured up through ground to the back plate by a Keithley 486 picoammeter gives a direct measure of the number of He* atoms.

4.2.3 Lithography Region

The Lithography region is a Kimball Physics MCF600-SC600800-A 6 inch spherical cube that is separated from the rest of the vacuum system by a Thermionics PFB-TLG-4000-H/R gate valve. The spherical cube has six 6 inch and eight 2.75 inch Conflat ports. Of the six 6 in ports: one is connected to the gate valve, one has a blank flange, one has an uncoated glass window that allows the optical mask to enter, one has a Nor-Cal ADV-600 quick access door which allows easy exchange of samples, one holds the two dimensional motorized stages, and one has a Conflat-to-Dependex converter which leads to a “T” which houses the cold trap as in Figure (4.6). The front two 2.75 inch conflat ports have 1 inch Huntington feed throughs attached to beam defining slits each with a 3 mm width. One of the slits has a 1 mm x 1 mm Copper mesh covering the opening of the slit. Two other 2.75 inch Conflat ports are used for electrical feed throughs for the motorized stages and the stainless steel detectors, and one 2.75 inch Conflat port has a residual gas analyzer attached. Figure (4.6) reviews the location of all the parts. Since [4], there have been two changes made to the lithography region. The spherical cube had two Nor-Cal ADV-600 quick access doors when the optical mask experiments at $\lambda = 1083.33$ nm were performed. An uncoated glass window replaced one of the Nor-Cal ADV-600 quick access doors because the $\lambda = 1083$ nm AR coating was significantly reducing the power of the experiments with an optical mask at 389 nm as discussed in Chapter 5. A cold trap was also added to decrease the amount of pumping time required between samples.

To change a sample requires the spherical cube to be opened. The Thermionics PFB-TLG-4000-H/R gate valve has a 2.75 inch inlet port which allows gas flow on one side of the valve. To bring the cube pressure up to atmosphere, dry nitrogen is flowed into this port until a Terranova gauge reads atmospheric pressure. The quick access door can then be opened and the sample changed. To pump down the cube, two sorption pumps are connected to the line attached to the inlet port. To maximize pumping speed, an alternate pump is cooled each time the system is pumped down. Once the pressure inside the spherical cube is about 10 mTorr, the sorption pumps are valved off and the Thermionics gate valve is slowly opened. The beam-line backing pressure of the turbo molecular pump is monitored and kept below 20 mTorr while opening the gate valve. After the valve is opened, the cold trap is filled with liquid nitrogen and the beam-line backing pressure decreases to the background pres-

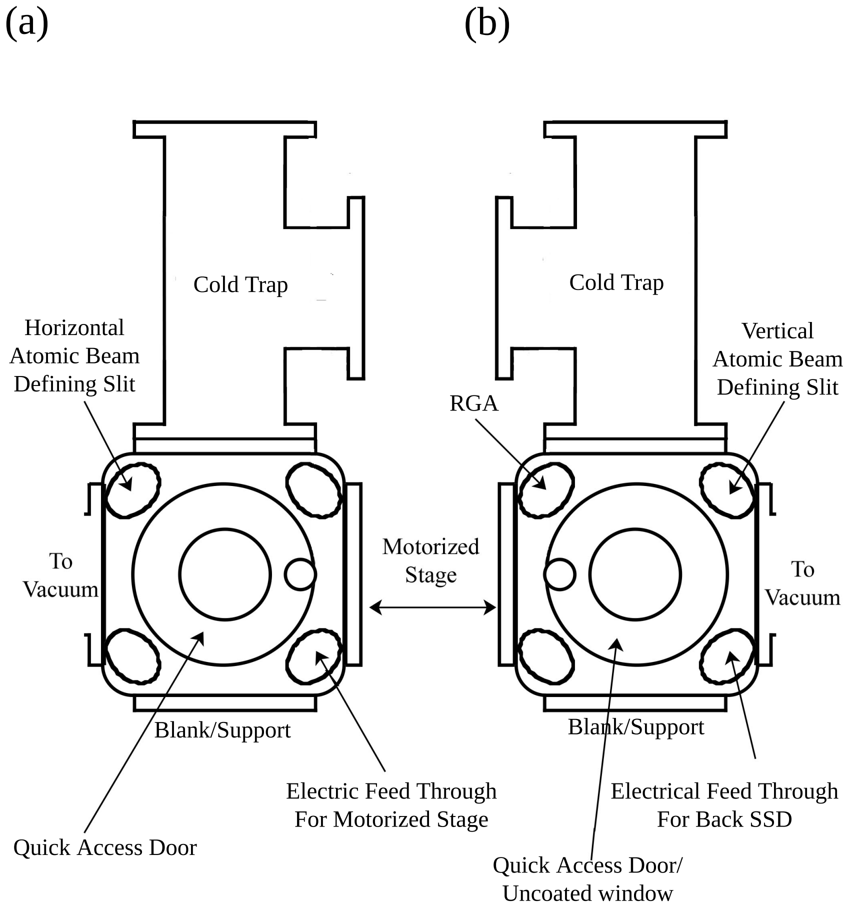

Figure 4.6: (a) A view of the spherical cube from the sample loading side (b) A view of the spherical cube from the incoming optical mask side. Note that the large 6 inch flange in (b) was a quick access door during experiments with the λ = 1083 nm optical mask and changed to an uncoated window during experiments with $\lambda = 389$ nm optical mask.

sure in a few minutes. Before installing the cold trap, it would take almost an hour before the backing pressure would return to the background value.

Motorized Stages

The farthest flange from the source (end flange of the spherical cube) holds two vacuum compatible miniaturized motorized National Aperture MM-3M-F-1.5-VAC stages which were installed in 2006. The stages are controlled by two MicroMini MVP1 Controllers that are computer controlled through an RS-232 interface. The stage program was written by Keller [21] in Visual Basic 6.0. The stages have a home-made Aluminum mount which is a rectangular block with grooves on the top and sides and is electrically grounded to the system. The grooves allow an upside down "U" shaped sample holder to be slid into place and remain steady.

Part of the stage program takes readings from the Keithley 486 picoammeter that are amplified in an Ithaco 1201 low-noise pre-amplifier and read by the computer through a National Instruments USB-6008 data acquisition card. The stages scan the atomic peak using a stainless steel detector mount described in the next section by moving in 0.5 mm steps over a 5 x 5 mm area. The stages move, allow time for the picoammeter to settle, average the readings and then plots the point. The same process is repeated without the atomic collimation and is considered to be background. The numbers are sent to a Mathematica notebook which calculates the time to achieve 3x10^{12} atoms/mm^2 at the peak. Recent plots of the peak can be seen in Figure (4.7).

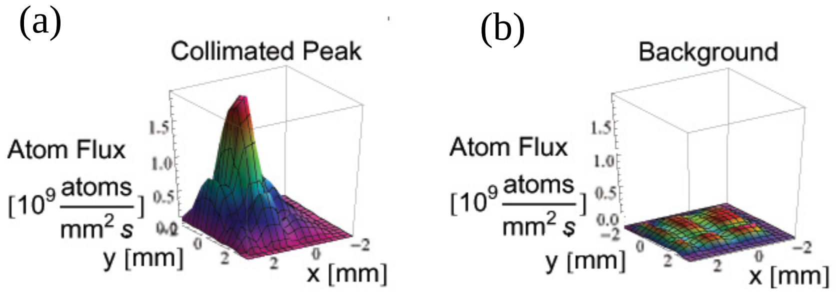

Figure 4.7: Recent back stainless steel detector scans of (a)the peak and (b) the background. The 1 mm x 1 mm mesh can be seen very well in the background scan.

Mounts

There are currently four mounts in use with the system in the spherical cube: a stainless steel detector mount, a sample mount with a mesh in front, a sample mount with a 1083 nm reflecting mirror, and a sample mount with a 389 nm reflecting mirror. The current sample holders are all mounted on a upside down "U" shaped holder that fits on the Aluminum block attached to the motorized stages as seen in Figure (4.8).

The stainless steel detector in the back operates on the same principle as the ones in front. The back stainless steel detector is made up of Kimball Physics C7X7 stainless steel and attached to the "U" shaped holder. The front plate has a 1 inch diameter hole covered by brass with a 0.456 mm diameter aperture and held at +250 V. The 0.456 mm hole was made by electrical discharge machining and the size was measured using the diffraction pattern created by a laser beam. The back plate is a just a stainless steel plate. Alumina rods, springs and retaining rings are used to hold the assembly together as seen in Figure (4.9) taken from Allred's thesis [4].

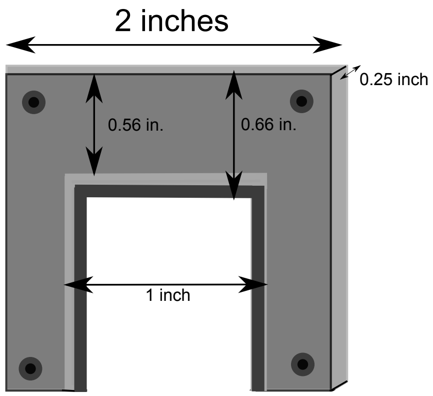

Figure 4.8: Every mount attaches to this "U" shaped holder that fits on the Aluminum block attached to the motorized stages.

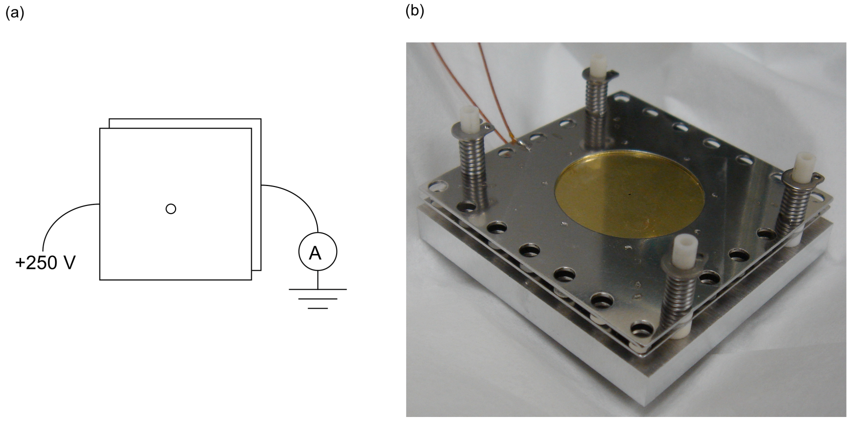

Figure 4.9: (a) Schematic of back stainless steel detectors (b) Experimental set-up of back stainless steel detectors

Figure 4.10: Sample mount used to expose boxes early in the experiment

Diagnostic tests to find the exact location of the sample mount relative to the stainless steel detector were done with a mount that has several pieces of SPI Supplies fine grid 1500 lines/inch mesh spot welded onto a C7x7 Kimball 2 inch plate with 1.5 inch diameter hole. As described in the next chapter, this mount was used to calibrate the system and can be seen in Figure (4.10).

The sample mount for the $\lambda = 1083$ nm optical mask is an un-anodized, specially lubricated, vacuum compatible ThorLabs KMS 100 mirror mount attached to the upside down "U" shaped holder. A right angle prism is attached to a 99.99 % reflective mirror at $\lambda = 1083$ nm by a thin layer of TorrSeal. A small aluminum piece holds a 4 x 12 mm sample up against the mirror as can be seen in Figure (4.11).

The sample mount for the $\lambda = 389$ nm optical mask follows the same design and uses a polarizing beam splitter cube attached via TorrSeal to a 99.9 %high

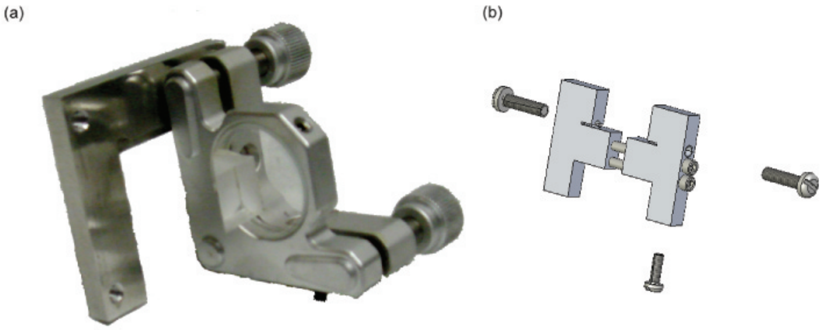

Figure 4.11: (a) The vacuum mount used for the optical mask exposures at 1083 nm. (b) 4 mm x 12 mm samples fit in the small groove and are held by the set screws on both sides. The piece is attached to the prism on the mirror such that the sample and mirror are perpendicular.

reflective mirror at $\lambda = 389$ nm. In later experiments with palladium, it was advantageous to use mesh to characterize the etch, and so a small piece was cut to fit in one end with the wafer and rest on top of the Aluminum on the other. The mount with and without the mesh can be in Figure (4.12).

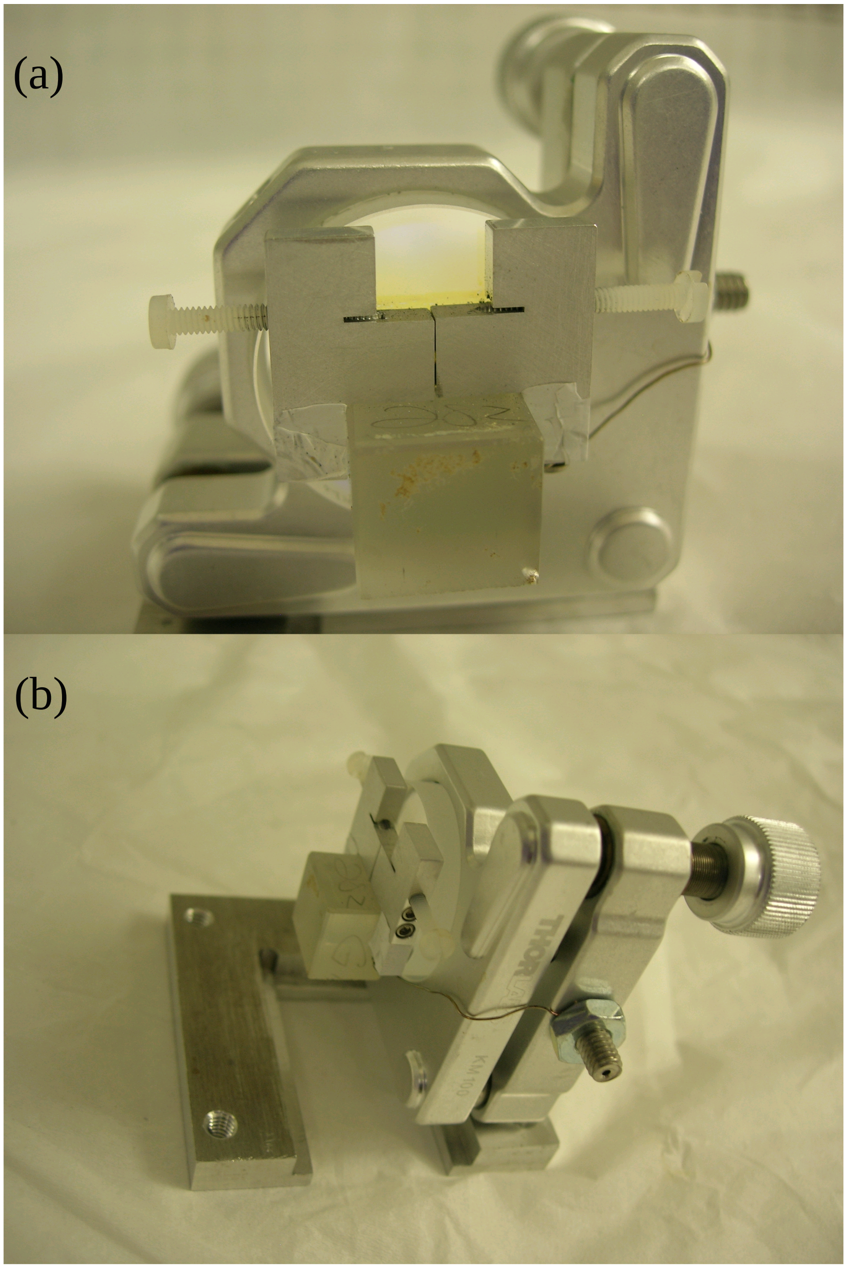

Figure 4.12: (a) The vacuum mount used for the optical mask exposures at 389 nm. The view is from the optical mask side. The sample is slid into the the grooves of the aluminum, with the gold facing up, and the nylon screws tightened.(b) This view of the mount shows how the “U” holder, the Thorlabs KMS-100 mirror mount and grounding wire.

Chapter 5

Lithography

5.1 Pattern Formation

To make structures on the sample, He* atoms are first used to damage a self-assembled monolayer (SAM) on a metallic layer. Patterning the beam of atoms prior to damaging the SAM is achieved by either using a mechanical mask or an optical mask as can be seen in Figure (5.1). Following the He* beam exposure, the sample is then placed in a selective wet chemical etch where the metal beneath the damaged SAM is removed, after which the samples are viewed with either an Atomic Force Microscope (AFM) or a Scanning Electron Microscope (SEM).

5.1.1 Mechanical Mask

The lithography experiments started with exposing samples to the He* beam while protected by a mechanical mask. The mechanical mask has been an invaluable tool to diagnose many problems that can occur in the experiment.

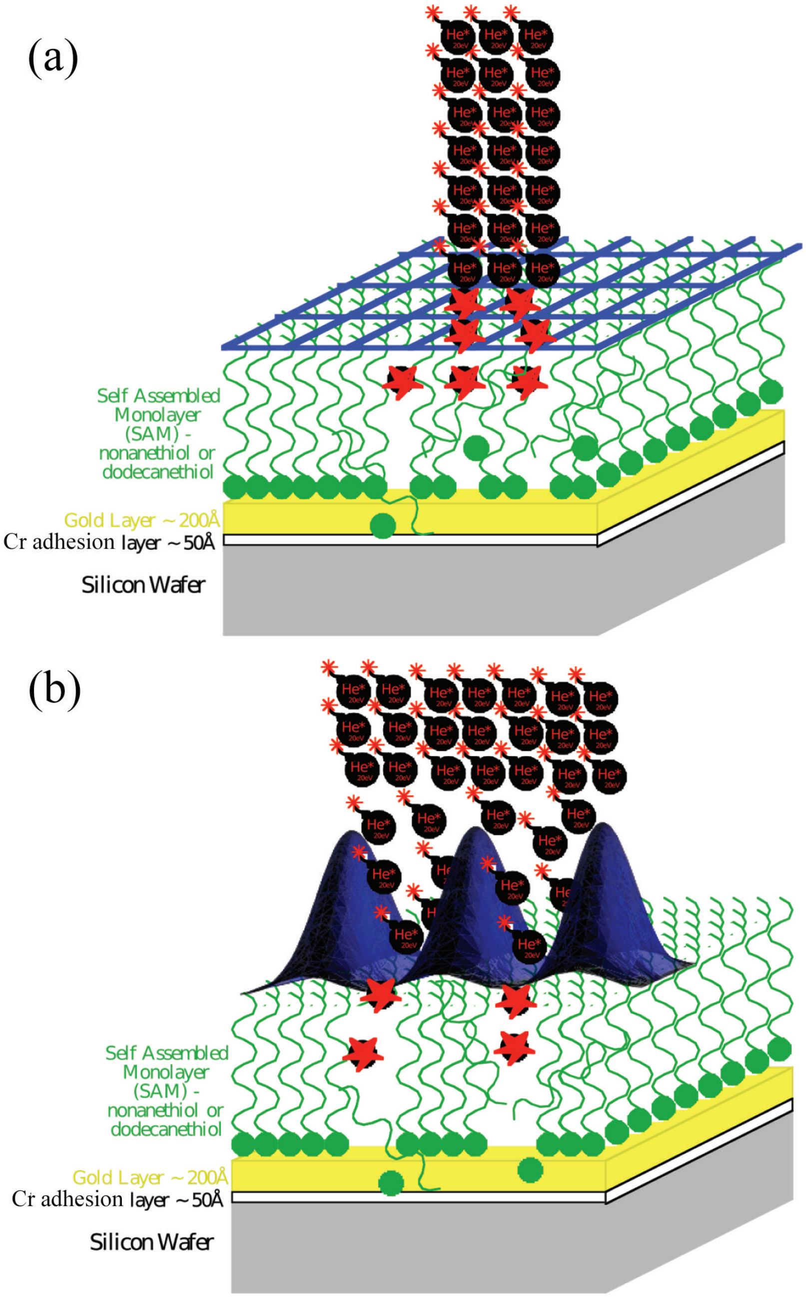

Figure 5.1: Figure (a) shows patterning with a mechanical mask. A shadow of the mask is made by removing the gold in areas that atoms have damaged the SAM. Figure (b) shows atoms being focused by the dipole force into lines using a standing wave of light.

Two 3 mm slits are attached to the 1 inch feed throughs in the front of the spherical cube as seen in Figure (4.6). The vertical slit has a 1 mm x 1 mm copper mesh across the open area to visibly mark the location of the He* beam on the sample during the etching procedure. Although the stages precisely measure the location of the He* beam peak and move the sample mount with a high degree of reproducibility, this is necessary because sample mount positions can vary up to 3 mm in the relative location of where the sample is held.

A finer mesh, with $\sim$ 11 μm squares and $\sim$16 μm periodicity, was used to determine the edge resolution that can be achieved by the etching process. These smaller boxes also have the added benefit of helping determine the He* beam dosage and etch times needed for optimal structure formation as discussed in subsection (5.4.1). The edge resolution is defined to be the distance between 90% and 10% positions of the feature height. AFM scans of the structure left by the shadow of the mechanical mesh were used to determine the average edge resolution over many AFM scans.

5.1.2 Optical Mask

The beam of He* atoms is focused into lines by a standing wave field of light detuned from the atomic transition frequency. The dipole force causes the atoms to be focused to the nodes or anti-nodes at the center of the standing wave depending on the sign of the detuning. There is a power parameter, independent of Gaussian beam size, that describes an optical mask beam that can focus atoms onto the axis of the standing wave. The incident power of the traveling wave that is retro-reflected to form the optical mask can be written in terms of this power parameter given by

$$P_{focus} = 5.37 \frac{\pi E_0 I_s \delta}{\hbar \gamma^2 k^2}. \tag{5.1}$$

Eq. (5.1) is taken from Eq. 23 of [32] for the case of a Gaussian laser beam, where E_0 is the longitudinal kinetic energy of an atom in a field free region. Since the optical mask in the current experiment is elliptical, rather than round as in Eq. (refeq:pfocus), the focusing power becomes $P'_{focus} = P_{focus}(w_{\|}/w_{\ell})$ where $w_{\|}$ is the waist of the beam parallel to the substrate surface and w_{ℓ} is the waist along the atomic beam path. P'_{focus} is the result of following the calculation in [32] and labeling the both axis of the laser beam.

The feature size of the lines created by the optical mask is dependent on the initial velocity or energy distribution of the incident atomic beam. To minimize the effects transverse velocity spread on the feature size, w_{ℓ} is kept small [33]. An added benefit of keeping w_{ℓ} small is that spontaneous emission of the atom in the light field becomes negligible [23].

Numerical simulations of focusing of atoms in standing wave light fields has previously been done [4, 32, 34, 35]. For the power in Eq. (5.1), the atomic trajectories bend smoothly to the center of the optical mask beam as seen in (a) of Figure (5.2).

If the incident beam that forms the standing wave has much more power than P'_{focus}, then it is denoted as the channeling region where experiments have previously been performed [36]. As the channeling regime is reached, the atomic trajectories cross the center of the focus many times. The power

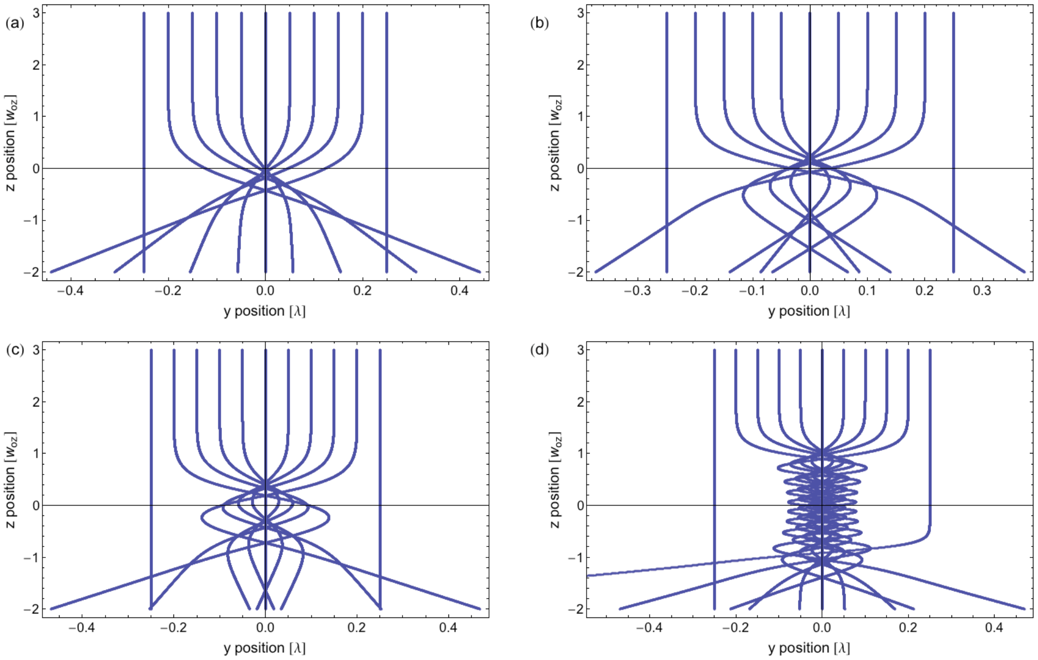

Figure 5.2: Numerical simulations from [4] that are in agreement with [32] show the trajectory of an atomic beam with no longitudinal chromaticity or divergence through a standing wave optical mask. The z=0 position corresponds to the center of the optical mask standing wave. (a) P_{inc}=P'_{focus}. (b)P_{inc}=2P'_{focus}. (c)P_{inc}=4P'_{focus}. (d) P_{inc}=64P'_{focus}

of our optical mask can be experimentally varied from P'_{focus} to well into the channeling regime [23]. Figure (5.2) shows the gradual transition of the atomic trajectories from the focusing to channeling regimes.

5.2 Gold Sample Preparation

The samples are built on single-crystal silicon wafers that have a 20 nm layer of gold evaporated onto their [100] surface over a 0.5 nm chromium adhesion layer. These 2 inch diameter wafers are purchased commercially from Montco Silicon Technologies who grows, cleans and polishes the silicon wafer. The 0.5 nm chromium adhesion layer followed by the 20.0 nm gold layer is e-beam evaporated onto the surface by Scientific Coatings.

AFM measurements show that the gold coating is not atomically smooth like the silicon wafer underneath. With such a thin layer of gold, the surface has granularity of ∼10's of nm and a surface roughness of a few nm. Annealing has been considered to help with the granularity and surface roughness, but has not been pursued.

The 2 inch wafers are diced into 4 mm by 12 mm rectangles with the help of Professor Luken's laboratory as they were in previous experiments [4]. A Microposit S1813 Photo Resist is spun on the gold wafer which is then mounted on 3M blue tape and cleaved by a diamond-and-epoxy resin blade in a Model 1006 Micro Automation programmable dicing saw.

To prepare the 4 mm by 12 mm wafers for a lithographic exposure, the Microposit S1813 Photo Resist is removed by acetone during a 10 minute treatment in an ultrasonic cleaner. The wafer is cleaned another 10 minutes in the ultrasonic cleaner while immersed in ethanol which removes the acetone and further cleans the surface. The wafer is then immersed in Piranha Solution (75% sulfuric acid, 25 % hydrogen peroxide) for 10 minutes to remove any remaining organic material on the gold surface. After the Piranha solution, the sample is ready to be coated with the SAM that forms the resist for patterning.

The SAM for the lithography exposures is formed onto the gold surface by submersing the wafer in a 1 mM solution of nonanethiol (Sigma-Aldrich, 1-Nonanethiol, technical $\geqq$ 99%) in ethanol (200 proof, ACS/USP grade, Pharmco Products Inc.). Experimentally, and in accord with similar experiments [36–38], 13 to 20 hours in solution was found to provide the most repeatable results even though 80% - 90% of the uptake of the thiol onto the gold surface happens in the first few minutes[39, 40]. The long chain molecules orient themselves with their hydrophillic heads bound to the gold substrate and their hydrophobic tails sticking out into the solution. At first the SAM molecules lie relatively flat, but as time passes more hydrophilic heads bind to the surface and a $(\sqrt{3}\times\sqrt{3})R30^\circ$ lattice structure is formed with the hydrocarbon chains tilted $\sim 33^\circ$ to the normal of the sample in an all trans orientation [4, 39].

5.3 Developing Structures in Gold

Once the SAM has formed on the surface, the sample is ready to be exposed to the He* beam. The sample is removed from the SAM solution, with PELCO SV Carbon Fiber Tweezers from Ted Pella to limit scratching, and dried with a light stream of dry nitrogen gas. The sample is slid into one of the three sample mounts described in Section (4.2.3) and the set screws are tightened to hold the sample in place. The mount is then placed in the vacuum system and the lithography region is pumped down.

5.3.1 Exposures

For exposures of a mechanical mesh, a sample is loaded into the sample mount with the mesh in front as seen in Figure (4.10), tightened to keep the sample in place, and the mount is placed in the vacuum system. The stages move the mount to the peak of the atomic beam and the sample is exposed to a dosage of $\sim 3 \times 10^{12}$ atoms/mm^2 [4, 20, 21] over the course of 30-40 minutes depending on the measured brightness of the He* beam after collimation.

For an optical mask exposure, more careful alignment is needed. First, the atomic beam and the optical mask need to be aligned perpendicularly to each other [36]. If the atoms have a large enough transverse velocity with respect to the potential created by the optical mask, there is a probability that the atoms will pass through several intensity peaks and valleys and not get focused.

To minimize this problem, the optical mask light is first aligned to the atomic collimation peak with the Doppler optical molasses blocked. The Doppler optical molasses and optical mask beams are aligned to the same height, and the spacing between the beams at the vacuum system are measured. Then a distance of ~3 m from the vacuum system, the height and spacing between each beam is again measured to ensure that the beams are parallel. Once aligned, the Doppler optical molasses is unblocked and steers the atomic beam to be at normal incidence to the optical mask.

Once the atomic beam is aligned to be perpendicular to the optical mask, the mirror mount sample holder is placed in the vacuum system and the KM-100 T mount adjusted until the incident light is retro-reflected. The light is initially aligned so that it is away from the sample and the retro-reflected optical power is measured using a polarizing beam splitter cube. Since the focusing happens at the middle of the Gaussian beam, two Newport 423 series translation stages are attached by a right-angle mount and hold a periscope that allows for horizontal translation of the optical mask beam. The optical mask is moved towards the sample until the power of the retro-reflected light reaches half of the initial value, then it is assumed that the sample is at the center of the optical mask beam.

Once aligned, the sample is exposed to $\sim 3 \times 10^{12}$ atoms/mm^2. Many atomic dosages were initially tested because focusing the atoms should have increased the dosage in the nodes of the optical mask. However, it is incredibly difficult to separate etching and dosage parameters [4] and this dosage provided repeatable results with repeatable etch times.

In either the mechanical or optical mask case, the incident He* attacks the structure of the SAM molecules thereby making them soluble in a wet chemical etch. The energetics of He* damaging the SAM molecules is not well understood. Studies with metastable Argon (Ar*) and He* indicate that deposition of the internal energy and secondary electron emission both contribute to weaken or break the SAM molecules [41]. For He*, the 20 eV per atom is roughly twice as large as the energy deposited by Ar*, while the dosage of He* required is 10-15 times less than that of Ar*, indicating that He* may have a different damage mechanism than metastable atoms with less energy [36, 41]. Further studies with He* show the 20 eV may be enough to break C-H or C-S bonds, increasing the wetability of the surface and allowing the etch to effectively remove the gold [42]. Although the damage mechanism is not clear, experimentally the He* definitely damage the SAM because of the results that have been obtained.

5.3.2 Etching the Gold samples

Once the sample has been exposed to the atomic beam, it is removed from the sample holder and immersed in a ferri/ferrocyanide based solution developed in 1995 [40]. This wet chemical etch ingredients are listed in Table (5.1).

Name	[mol/l]	Amount	Manufacturer
Potassium Hydroxide	1	15.586 g	Fisher Scientific
Potassium Thiosulfate	0.1	4.758 g	Riedel-de Haën
Potassium Ferricyanide (III)	0.01	0.823 g	Sigma-Aldrich
Potassium Ferrocyanide (II) Trihydrate	0.001	0.106 g	Sigma-Aldrich
Distilled Water	solvent	250 ml	Chemistry Stockroom

Table 5.1: Chemicals are weighed using a lab scale with an accuracy of ±2 mg.

The sample is placed in a petri dish containing the etching solution large enough to accommodate a magnetic stirrer, a thermometer and some space around the sample for easy access with the tweezers. The magnetic stirrer is turned on to $\sim$ 200 rpm to get a more uniform etch while stirring the solution slowly enough so that the sample can sit on the bottom of the petri dish.

A two step electrochemical process consisting of (1) metal oxidation (dissolution)

$$\mathrm{Au}^0 + 2\mathrm{S_2O_3}^{2-} \rightarrow \mathrm{Au}\left(\mathrm{S_2O_3}\right)_2{}^{3-} + e^- \tag{5.2a}$$

or

$$\begin{aligned} \mathrm{Au}^0 + 2\mathrm{OH}^- &\rightarrow \mathrm{Au}\left(\mathrm{OH}\right)_2{}^- + e^- \\ \mathrm{Au}\left(\mathrm{OH}\right)_2{}^- + 2\mathrm{S_2O_3}^{2-} &\rightarrow \mathrm{Au}\left(\mathrm{S_2O_3}\right)_2{}^{3-} + 2\mathrm{OH}^- \end{aligned} \tag{5.2b}$$

and (2) reduction of an oxidizer

$$\mathrm{Fe}\,(\mathrm{CN})_6{}^{3-} + e^- \rightarrow \mathrm{Fe}\,(\mathrm{CN})_6{}^{4-} \tag{5.3}$$

etches the structures permanently in the gold. The rate of the chemical process is dependent on many different parameters, including exposure dosage, chemical concentrations and temperature. The etch time is determined by immersing the sample in the etch solution until the shadow of the 1 mm x 1 mm grid that is on the beam defining slit starts to become visible. Once the square pattern can be seen by eye, the time is noted and the sample is left etching for 35% longer. Most recently, the squares consistently appear after ~2 minutes and the total etch time is around ~3 minutes.

After being removed from the etch, the sample is rinsed with distilled water and then ethanol. Dry Nitrogen gas is used to dry the sample to prevent spotting. Then the sample can be analyzed using the AFM in our lab. Or, if the sample is going to the Zeiss/LEO 1550 Schottky Field Emission Gun scanning electron microscope (SEM) housed in the Materials Science department at Stony Brook University, it is first cleaned in Piranha Solution, then water, then ethanol. If the extra cleaning of the wafer is not done, SAM residue can be seen during SEM scans.

5.4 Results in Gold

5.4.1 Boxes

The first samples were exposed using a SPI 1500 lines/inch nickel mesh as a mechanical mask. The etched boxes were used to determine the appropriate He* dosage and the etching edge resolution. The results for both He* dosage and etching edge resolution were similar to previous experiments using He* and mechanical meshes [41, 43–45]. Two independent analyses show that the edge resolution is on average ∼80 nm over many AFM scans. One such measurement can be seen in Figure (5.3). The edge resolution did not change appreciably when exposure dosage was varied, and is mostly limited by the isotropic nature of the etch with contributions from the granularity of the gold.

The boxes also help to understand the exposure parameters. For example, evidence of etching in areas protected by the mechanical mask indicate that the sample was over-etched. Having gold left inside an etched square is an indicator of under-etching. Under-exposure leads to long etch times and break through etching in the area protected by the mesh. Over-exposure usually results in extremely short etching times. These indicators are not independent of each other, which makes it difficult to find a good set of parameters.

5.4.2 Lines with 1083 nm light

Our beam of He* atoms is focused into lines by a standing wave light field of λ = 1083 nm light detuned ∼490 MHz above the $2^3S_1 \rightarrow 2^3P_2$ transition (atoms

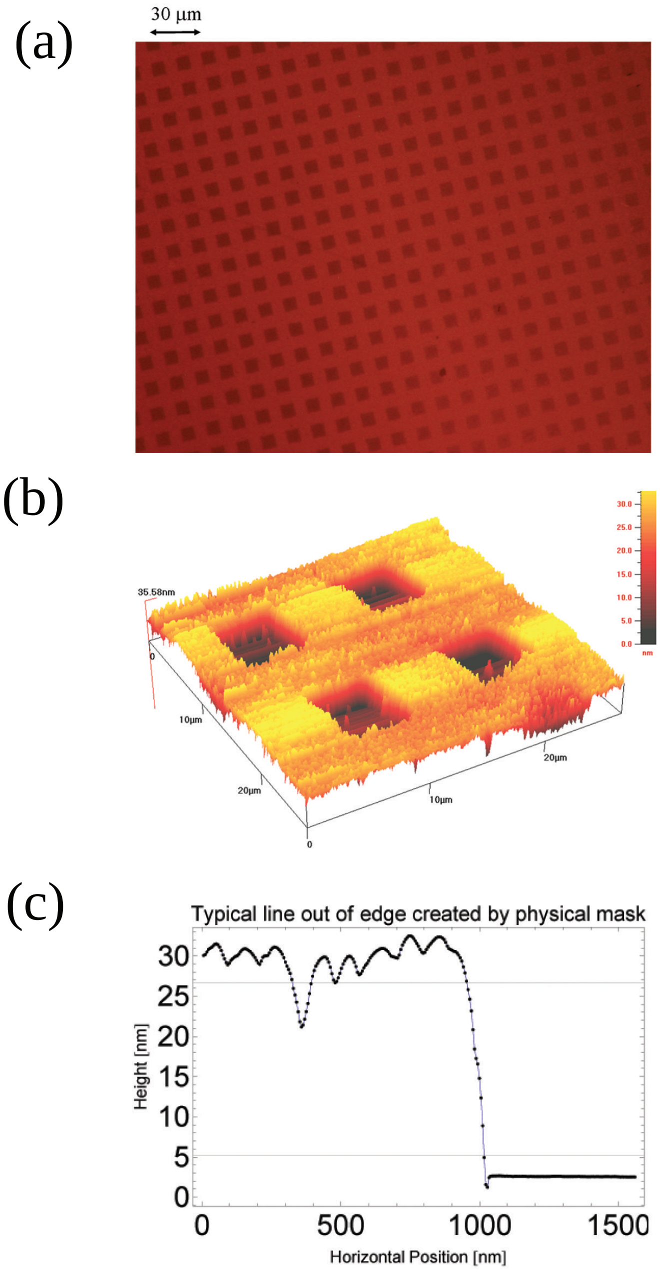

Figure 5.3: (a)Reflecting light microscope picture of boxes etched in gold after exposure to He* protected by a mechanical mask. (b) Three dimensional AFM image of boxes etched in gold. (c) Line out from AFM to show the edge resolution.

attracted toward its nodes). The optical mask has an elliptical cross section with a waist of $w_{\parallel} \sim 1.5$ mm parallel to the sample surface and $w_{\ell} \sim 330\,\mu$m along the atomic beam path. The light is circularly polarized and its power can be varied with the Optocom 1 Watt fiber amplifier from P'_{focus} to well into the channeling regime.

Channeling Regime

The edge resolution of 80 nm is sufficiently small that the etching process should be able to produce lines spaced by 541 nm in gold. Samples patterned with an optical mask in the channeling regime produced the expected array of lines covering the full 3 × 3 mm exposed region of the sample. The entire area is quite uniformly patterned as seen in both AFM and SEM scans. Figure (5.4) shows the lines that are spaced 541 nm apart. The power of the optical mask beam used for this sample was $\sim 14\,\text{mW} \approx 2.8P'_{focus}$.

Figure (5.4) shows that the depth of the lines is approximately 10 nm and that the spatial patterning resolution is limited by the gold graininess to about 1/5 of the line separation, ∼100 nm. Typical samples were exposed with the optical mask at a power of $2.8P'_{focus}$, but the lines were achieved with optical mask powers as high as $10P'_{focus}$ to compare with [34].

Focusing Regime

We are the first to demonstrate patterning with He* using an optical mask in the focusing regime. The power of the beam used to form the structures shown in Figure (5.5) was $\sim P'_{focus} \approx 5.0$mW and the exposure time was ∼48 minutes corresponding to 3 x 10^{12} atoms/mm^2. Patterning in the focusing regime is

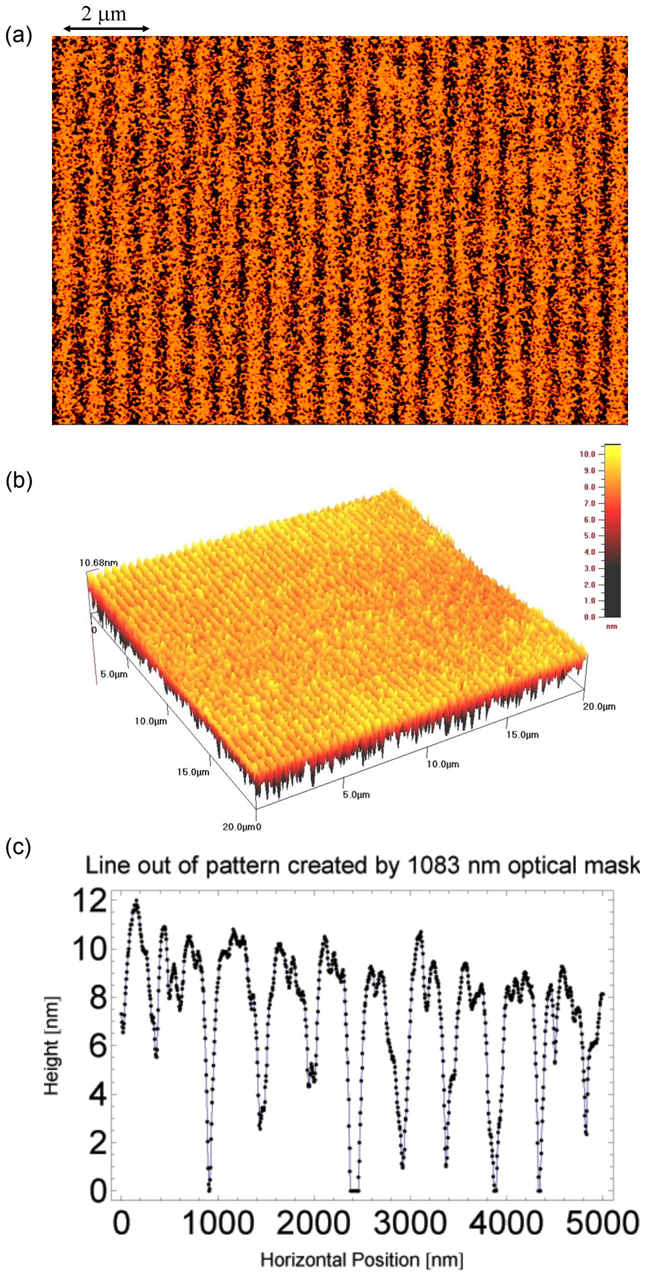

Figure 5.4: (a)False color SEM image of lines focused by an optical mask in the channeling regime. (b) Three dimensional AFM image of lines made by an optical mask in channeling regime. (c) Line out from (b) to show the relative depth and shape of typical lines.

difficult because many He*, due to their transverse or longitudinal velocities, do not get focused properly causing less contrast in dosage between the nodes and anti-nodes. Although not as well defined as the channeling regime, the images still show lines at the correct spacing.

5.4.3 Lines with 389 nm Light

Another first for this experiment is the demonstration of lines in gold that are separated by 194.5 nm as seen in Figure (5.6). This is achieved by using a 388.98 nm optical mask that is detuned 80 MHz below $2^3S_1 - 3^3P_2$ atomic transition. It is interesting to note that the sign of the detuning has changed, and that now the atoms are focused toward the high light intensity in this experiment. The optical mask again has an elliptical Gaussian shape now with $w_{\|} = 1.12$ mm and $w_{\ell} = 0.18$ mm.

Lines were created first by circularly polarized and then by linearly polarized light in the optical mask. The polarization was switched to try to increase the contrast of the focused atoms to the non-focused atoms by taking advantage of the transition strengths of the different m$_J$ states. The focusing power stated in Subsection (5.1.2) is calculated on the strongest transition (m$_J$=1 to m$_J$=2) as seen in Figure (5.7). After collimation, the He* atoms travel in a field-free path where the atoms equally populate the three ground state m$_J$ states. This means only 1/3 of the atoms see the highest relative transition strength for circularly polarized light. If linearly polarized light is used all the atoms feel roughly the same focusing force.

When the optical mask was circularly polarized, it was easy to monitor the

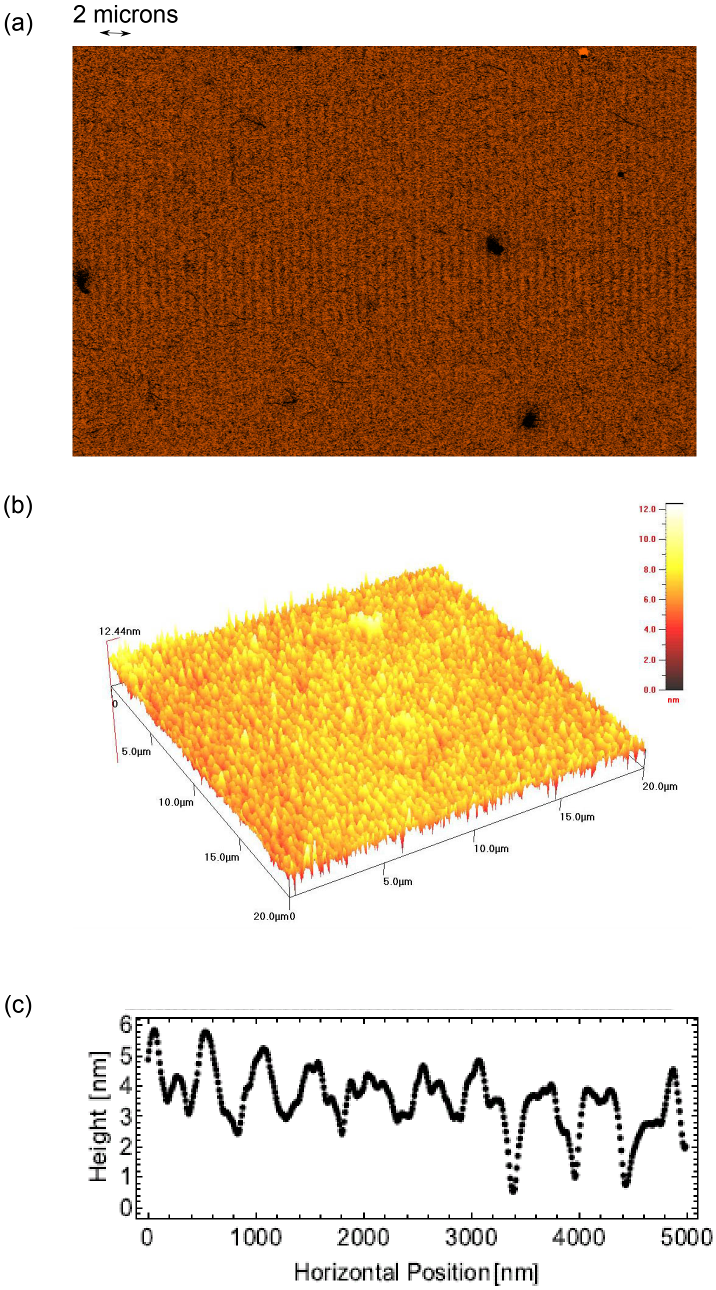

Figure 5.5: (a)False color SEM image of lines in the focusing regime. (b) Three dimensional AFM image of lines made by optical mask in focusing regime. (c) Line out averaged over 1 μm of (b) from AFM to show the relative depth and shape of typical lines in the focusing regime.

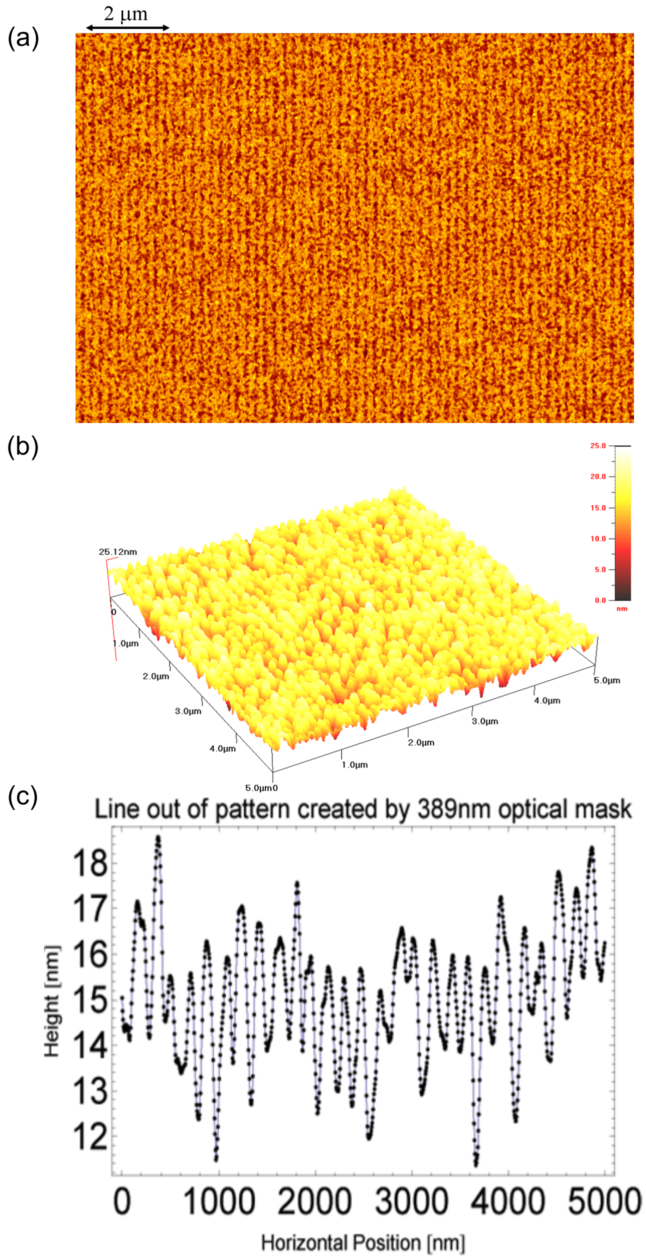

Figure 5.6: (a)False color SEM image of lines created with 389 nm optical mask. (b) Three dimensional AFM image of lines made by 389 nm optical mask. With the spacing so close, the granularity of the gold makes lines very hard to see (c) Line out from AFM to show the relative depth and shape of typical lines made by the 389 nm optical mask.

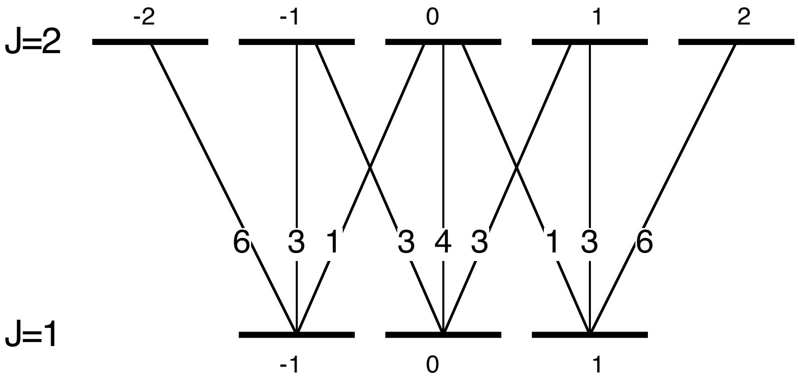

Figure 5.7: The hyperfine levels of the J=1 to J=2 states with their relative transition strengths.

retro-reflected light as the reflected light would be orthogonally polarized to the incoming light because of the quarter wave plate. To align the linear polarized light, the polarizing beam splitter cube and quarter wave plate were replaced by a microscope slide in the laser beam. The microscope slide allowed the retro-reflected beam to be picked off and monitored for alignment purposes. Lines were made with both linearly and circularly polarized light. Unfortunately, due to the granularity of the gold and the limits of the isotropic etching no noticeable difference was seen in final structures.

5.5 Analysis of Lines

Analysis of the samples with lines begins with spatial Fourier transforms of the images from both AFM and SEM scans. Fast Fourier Transforms (FFT) are used to find features that may be hard to see by eye, and also to understand the shapes of the lines in the periodic arrays. Even in samples where the pattern is difficult to see in the images, the peaks in the FFT's clearly reveal the presence of the lines.

These transforms allow the spacing between the lines to be easily measured, but the numerical results are subject to the calibration of the instrument. For example, the AFM is calibrated by scanning an array of lines of 1 μm spacing. Needless to say, the spectroscopically known accuracy of our line spacing is significantly higher than that of the calibration samples provided by the microscope manufacturer. The FFTs of the scans from both the AFM and SEM consistently show the same set of higher harmonics, with approximately the same relative amplitudes, indicating that the overall shape of the patterns is not greatly affected by the power of the light mask.

Figure (5.8) shows typical FFTs in the dimension across the lines. All the samples have a strong fundamental harmonic. The second harmonics can be seen in the channeling regime and quickly disappear as the lines get less noticeable by eye as in the 389 nm optical mask.

5.6 Palladium Sample Preparation

The gold sample patterns are limited by both the surface granularity and etching procedure, so research into palladium samples began. Thin layers of palladium have much smaller grain sizes (15-25 nm) than thin layers of gold (50-100 nm)[46] and the nonanethiol that acts as the resist will still grow on the surface [46–48]. Since the current set-up produces lines repeatedly, switching the sample and etching solution seemed to be advantageous.

The silicon wafers are coated with palladium with help from Bent Nielson in the neighboring laboratory. Wafer World provides the 2 inch diameter, p-type,

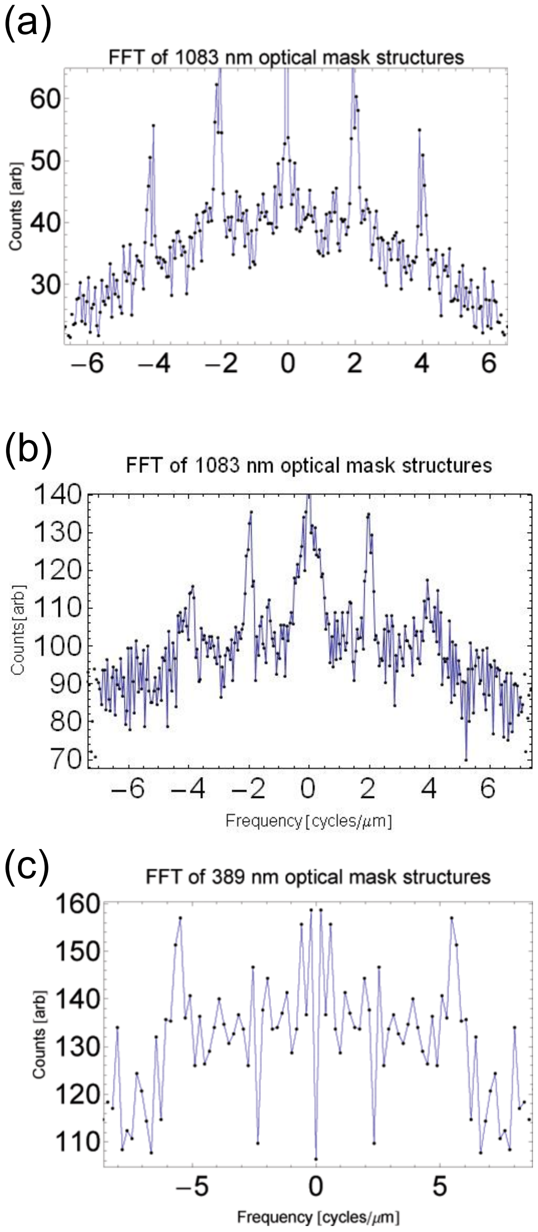

Figure 5.8: (a)Shows the FFT of 541 nm spaced lines created with an optical mask in the channeling regime. The strong second harmonics show that the lines are relatively flat on top and have sharp trenches. (b) Shows the FFT of 541 nm spaced lines created with an optical mask in the focusing regime. As can be seen from the line out in Figure (5.5) the pattern is much closer to sinusoidal and the second harmonics are suppressed. (c)Shows the FFT of 194.5 nm spaced lines. Although the microscope images do not clearly show the pattern of lines, the fundamental harmonic is clearly visible.

silicon wafer that has a [100]± 1° orientation, a resistivity of 1-20 Ohm-cm and a thickness of 250-300 microns. The silicon is put in a high vacuum chamber of $\sim 10^{-7}$ Torr and a 0.5 nm layer of chromium is evaporated via electron-beam onto the surface, followed by $\sim$ 25 nm of 99.95% pure palladium from Kurt J. Lesker company. The silicon wafer is held about a meter away from the evaporation source and AFM analysis has shown that the coating thickness is uniform across the sample.

The sample is then sent to the Luken's lab to be diced. Again, a Microposit S1813 Photo Resist is spun on the surface, and then wafer is mounted on 3M blue tape and cleaved by a diamond-and-epoxy resin blade in a Model 1006 Micro Automation programmable dicing saw to make 4 mm x 12 mm samples.

Before an exposure, samples are cleaned for 10 minutes in an ultrasonic cleaner while immersed in acetone followed by another 10 minutes in an ultrasonic cleaner while immersed in ethanol. The palladium wafers are not placed in Piranha solution because the solution dissolves Palladium at a rate of $\sim$3 nm/min [49].

As a side note, it was not known to us that Piranha solution dissolves palladium until etch tests were done. After immersing a palladium sample in Piranha solution only the chromium layer was left. It was found that the gold etch effectively removes the chromium layer and confirmed that a good etch in gold goes all the way down to the silicon wafer.

After being cleaned in ethanol, the samples are transferred into a 1 mM solution of nonanethiol (Sigma-Aldrich, 1-Nonanethiol, technical $\geqq$ 99%) in ethanol (200 proof, ACS/USP grade, Pharmco Products Inc.). Exposing a palladium wafer coated with nonanethiol to a beam of metastable atoms had never been done, so the SAM was allowed to form for 13-20 hours based on knowledge from the gold samples. The SAM is more tightly packed when it forms on palladium [46]. Experiments have also been done with a SAM solution of dodecanethiol (Sigma-Aldrich, 1-Dodecanethiol,technical $\geqq$ 95%) as previous experiments in the lab suggest that the dodecanethiol better resists break through etching at the cost of higher atom dosages.

5.7 Developing Structures in Palladium

For the palladium wafers, a mechanical mask was used by placing a small piece of SPI nickel mesh over the sample on the 388.98 nm optical mask mount. The samples were exposed to 3×10^{12} atoms/mm^2 as that is what worked best in gold exposures. Many atomic dosages were tried, but this particular dosage has high repeatability in producing structures.

The sample is removed from the vacuum system and place in 50°C diluted (125 parts distilled water: 1 part etch solution) Palladium TFP etch from Transene Company which is composed of 25-35% ferric chloride, $3-4\%$ hydrochloric acid and ≥ 60 % water by weight. The non-dilute etch is specified to have an etch rate of 11.0 nm/s at 50°C. Diluting the solution provides etch times of 2-3 minutes for the samples.

5.8 Results in Palladium

The samples in palladium were exposed using a nickel mesh as a mechanical mask. The edge resolution for the boxes etched into palladium was ~120 nm for feature heights of ~38 nm. When adjusted for the height difference from gold, the edge resolution is comparable. A notable exception is that the palladium etching process causes a circular feature to be seen around any edges as in Figure (5.9). It has been suggested that the circles are formed because there are impurities on the surface of the palladium. Since the impurity allows the etch to start immediately, the isotropic nature causes the circular shape.

Unfortunately, the impurities on the surface may be damaged SAM. Work has been done, including exploring an unsuccessful two step etch, to limit the size of the circles. Figure (5.9) shows boxes made under standard exposure conditions with nonanethiol and then with dodecanethiol used as the resist.

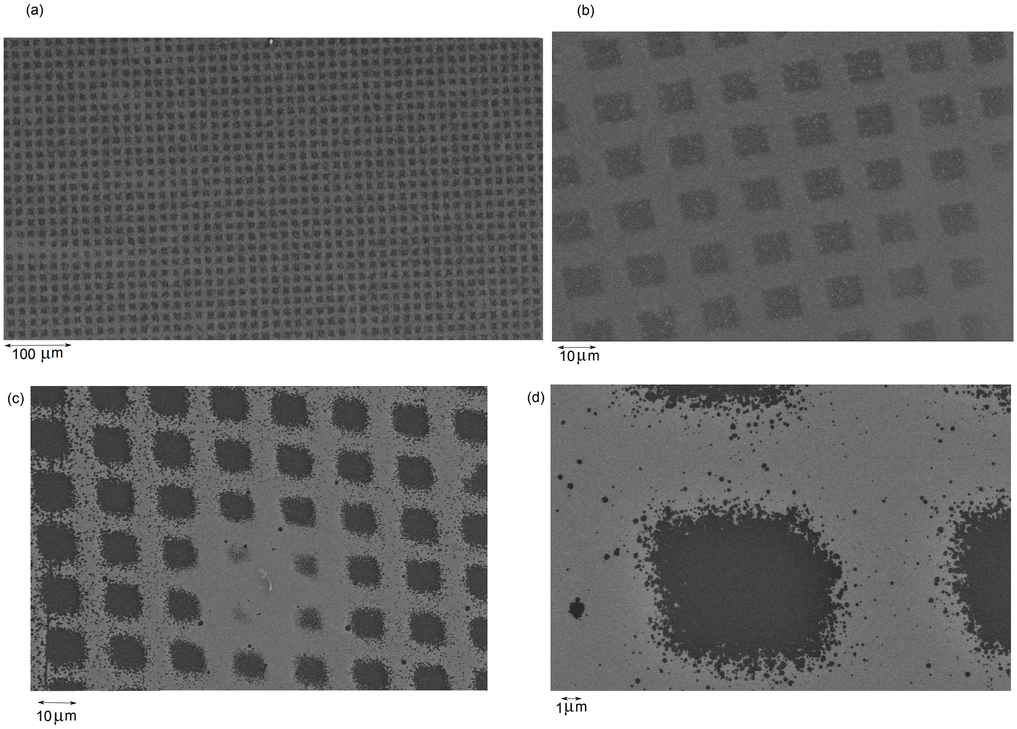

Figure 5.9: (a)Large scale patterning is easily done in using a mechanical mesh with a nonanethiol resist. (b) Another nonanethiol resist zoomed in so the edge pattern can be seen. (c) Dodecanethiol resist with many boxes present. The sample is slightly over-etched as there is break through etching under the shadow of the mask. (d)A close view of the box edge. Here the small circular features can be seen. All images were taken with an SEM.

Chapter 6

Conclusion

Our fabrications have been reliable and repeatable, sample after sample, over a period of months. Creating patterns with a mechanical mesh has a very high success rate and covers the entire region exposed by the beam defining slits. In a standing wave arranged to channel the He* into lines separated by $\lambda/2$ on the sample, our lines cover the entire exposed length of the substrate, about 3 mm and to about twice the beam waist of the laser standing wave.

The method has been demonstrated using both 1083.33 nm light and 388.98 nm light as masks. Results have been achieved in the channeling and focusing regime for 1083.33 nm light and in the focusing regime for the 388.98 nm light. The atoms were focused into the node and in separate experiments to the anti-nodes of the optical mask. Results have been achieved with both linearly and circularly polarized light. After nearly a year, samples were analyzed under our AFM once again and still showed similar features to the first scans.

The first exposures in palladium serve as proof of principle that this lithographic technique can be expanded to other materials that are more suitable to make small structures.

Future ideas for this experiment include attempting to make lines in palladium. Two dimensional structures may also be pursued.

Bibliography

[1] M. Prentiss, G. Timp, N.Bigelow, R.E. Behringer, and J.E.Cunningham. Using light as a stencil. *Appl. Phys. Lett.*, 60(8):1027–1029, 1992.

[2] J. J. McClelland, R.E. Scholten, E.C. Palm, and R.J. Celotta. Laser-focused atomic deposition. *Science*, 262(5135):877–880, 1993.

[3] K.K. Berggren, A. Bard, J.L. Wilbur, J.D.Gillaspy, A. Helg, J.J. McClelland, S.L.Rolston, W.D. Phillips, M.Prentiss, and G.M. Whitesides. Microlithography by using neutral metastable atoms and self-assembled monolayers. *Science*, 269(5228):1255–1257, 1995.

[4] C.S. Allred. *Neutral Atom Lithography with Metastable Helium.* Ph.D. thesis, SUNY Stony Brook, Stony Brook, NY, May 2009.

[5] D.J. Griffiths. *Introduction to Quantum Mechanics.* Prentice Hall, New Jersey, 1994.

[6] J.J. Sakurai. *Modern Quantum Mechanics.* Addison-Wesley, Singapore, 1994.

[7] H.A. Bethe and E.E. Salpeter. *Quantum Mechanics of One- and Two-Electron Atoms.* Dover Publications, Inc., Mineola, NY, 2008.

[8] J.R. Woodworth and H.W. Moos. Experimental determination of the single-photon transition rate between the 2^3S_1 and 1^1S_0 states of He I. *Phys. Rev. A*, 12:2445, 1975.

[9] G. Lach and K. Pachucki. Forbidden transitions in the helium atom. *Phys. Rev. A*, 64(042510), 2001.

[10] H.J. Metcalf and P. van der Straten. *Laser Cooling and Trapping.* Graduate Texts in Contemporary Physics. Springer, Berlin, 1999.

[11] C.J. Foot. *Atomic Physics*, volume 7 of *Oxford Master Series in Physics.* Oxford University Press, Oxford, UK, 2005.

[12] R. Feynman, F. Vernon, and R. Hellwarth. Geometrical representation of the Schrödinger equation for solving maser problems. *J. App. Phys.*, 28: 49, 1957.

[13] P. Meystre and M. Sargent III. *Elements of Quantum Optics.* Springer, New York, 2007.

[14] P.W. Milonni and J.H. Eberly. *Lasers.* John Wiley and Sons, Inc., New York, 1988.

[15] P. Meystre. *Atom Optics*, volume 33 of *Springer Series on Atomic, Optical and Plasma Physics.* Springer, Berlin, 2001.

[16] S. Stenholm, V.G. Minogin, and V.S. Letokhov. Resonant light pressure due to a strong standing wave. *Opt. Comm.*, 25(1):107–110, 1978.

[17] V.G. Minogin and O.T. Serimaa. Resonant light pressure forces in a strong standing laser wave. *Opt. Comm.*, 30(3):373–379, 1979.

[18] M.T. Cashen. *Optical Forces on Atoms in Polychromatic Light Fields.* Ph.D. thesis, SUNY Stony Brook, Stony Brook, NY, May 2002.

[19] M.J. Partlow. *Bichromatic Collimation to Make an Intense Helium Beam.* Ph.D. thesis, SUNY Stony Brook, Stony Brook, NY, December 2004.

[20] M.P. Riedmann. Neutral atom lithography using a beam of metastable helium collimated by bichromatic light. Master's thesis, SUNY Stony Brook, Stony Brook, NY, August 2005.

[21] M.C. Keller. Optical manipulation of helium atoms with application to neutral atom lithography. Master's thesis, SUNY Stony Brook, Stony Brook, NY, August 2006.

[22] H.J. Metcalf. Entropy exchange in laser cooling. *Phys. Rev. A*, 77:061401, June 2008.

[23] C.S. Allred, J. Reeves, C. Corder, and H. Metcalf. Atom lithography with metastable helium. *Journal of Applied Physics*, 107(033116), 2010.

[24] M.R. Williams. *Measurement of the Bichromatic Force on Rubidium Atoms.* Ph.D. thesis, SUNY Stony Brook, Stony Brook, NY, August 1999.

[25] S.H. Lee. *Coherent Manipulation of Rydberg Helium Atoms in Inhomogenous Electric Fields.* Ph.D. thesis, SUNY Stony Brook, Stony Brook, NY, August 2006.

[26] R.W.P. Drever, J.L. Hall, F.V. Kowalski, J. Hough, G.M. Ford, A.J. Munley, and H. Ward. Laser phase and frequency stabilization using an optical resonator. *Appl. Phys. B*, 31:97–105, 1983.

[27] T.W. Hänsch and B. Couillaud. Laser frequency stabilization spectroscopy of a reflecting reference cavity. *Optics Communications*, 35(3): 441, 1980.

[28] J. Kawanaka, M. Hagiuda, K. Shimizu, F. Shimizu, and H. Takuma. Generation of an intense low-velocity metastable-neon atomic beam. *Appl. Phys. B: Lasers Opt.*, 56:21–24, 1993.

[29] H.C. Mastwijk, J.W. Thomsen, P. van der Straten, and A. Niehaus. Optical collisions of cold, metastable helium atoms. *Phys. Rev. Lett.*, 80(25): 5516–5519, June 1998. ISSN 0031-9007.

[30] J.L. Wiza. Microchannel plate detectors. *Nuclear Instruments and Methods*, 162:587–601, 1979.

[31] F. B. Dunning, R. D. Rundel, and R. F. Stebbings. Determination of secondary electron ejection coefficients for rare gas metastable atoms. *Rev. Sci. Instrum.*, 46(6):697–701, 1975.

[32] J.J. McClelland. Atom-optical properties of a standing-wave light field. *J. Opt. Soc. Am. B.*, 12(10):1761–1768, October 1995.

[33] D. Meschede and H. Metcalf. Atomic nanofabrication: atomic deposition and lithography by laser and magnetic forces. *J. Phys. D: Applied Phys.*, 36:R17–R38, Jan 2003.

[34] S. Petra. *Nanolithography with metastable helium atoms.* Ph.D. thesis, Vrije Universiteit, Amsterdam, June 2004.

[35] K.K. Berggren, M. Prentiss, G.L. Timp, and R.E. Behringer. Calculation of atomic positions in nanometer-scale direct-write optical lithography with an optical standing wave. *J. Opt. Soc. Am. B.*, 11(7):1166–1176, October 1994.

[36] P. Engels, S. Salewski, H. Levsen, K. Sengstock, and W. Ertmer. Atom lithography with a cold, metastable neon beam. *Appl. Phys. B.*, 69:407–412, 1999.

[37] L.P. Ratliff, R. Minniti, E.W. Bell, J.D. Gillaspy, D. Parks, A.J. Black, and G.M. Whitesides. Exposure of self-assembled monolayers to highly

charged ions and metastable atoms. *Appl. Phys. Letters*, 75(4):590–592, 1999.

[38] S. Petra, L. Feenstra, W. Hogervorst, and W. Vassen. Nanolithography with metastable helium atoms in a high-power standing-wave light field. *Appl. Phys. B.*, 78:133–136, 2004.

[39] F. Schreiber. Structure and growth of self-assembling monolayers. *Prog. Surf. Sci.*, 65:151–256, 2000.

[40] Y. Xia, Z.M. Zhao, E. Kim, and G. Whitesides. A selective etching solution for use with patterned self-assembled monolayers of alkanetiolates on gold. *Chem. Mater.*, 7:2332–2337, 1995.

[41] A. Bard, K.K. Berggren, J.L. Wilbur, J.D. Gillaspy, S.L Rolston, J.J. McClelland, W.D.Phillips, M. Prentiss, and G.M. Whitesides. Self-assembled monolayers exposed by metastable argon and metastable helium for neutral atom lithography and atomic beam imaging. *J. Vac. Sci. Technol. B*, 15(5):1805–1810, 1997.

[42] J.D. Close, K.G.H. Baldwin, K. Hoffmann, and N. Quass. Fragmentation of dodecanethiol molecules: application to self-assembled monolayer damage in atom lithography. *Appl. Phys. B*, 70:651–655, March 2000.

[43] S. Nowak, T. Pfau, and J. Mlynek. Nanolithography with metastable helium. *Appl. Phys. B.*, 63:203–205, 1996.

[44] B. Brezger, Th. Schulze, U. Drodofsky, J. Stuhler, S. Nowak, T. Pfau, and J. Mlynek. Nanolithography with neutral chromium and helium atoms. *J. Vac. Sci. Technol. B*, 15(6):2905–2911, 1997.

[45] A.S. Bell, T. Pfau, U. Drodofsky, T. Stuhler, Th. Schulze, B. Brezger, S. Nowak, and J. Mlynek. Atomic lithography. *Micro. Elec. Eng.*, 41: 587–590, 1998.

[46] J.C. Love, D.B. Wolfe, M.L. Chabinyc, K.E. Paul, and G.M. Whitesides. Self-assembled monolayers of alkanethiolates on palladium are good etch resists. *J. Am. Chem. Soc.*, 124(8):1576–1577, 2002.

[47] D.B. Wolfe, J.C. Love, K.E. Paul, M.L. Chabinyc, and G.M. Whitesides. Fabrication of palladium-based microelectronic devices by microcontact printing. *Appl. Phy. Lett.*, 80(12):2222–2224, 2002.

[48] H. Zhang and C.A. Mirkin. Dpn-generated nanostructures made of gold, silver, and palladium. *Chem. Mater.*, 16:1480–1484, 2004.

[49] K.R. Williams, K. Gupta, and M. Wasilik. Etch rates for micromachining processing part ii. *Journal Of Microelectromechanical Systems*, 12(6): 761–778, 2003.